



INSTITUTO SUPERIOR DE ENGENHARIA DE LISBOA

Área Departamental de Engenharia Electrónica
e Telecomunicações e de Computadores

A Biosignal Embedded System for Physiological Computing

José Guerreiro

(Degree in Electronic and Telecommunications
and Computers Engineering)

Thesis submitted in the fulfilment of the requirements for the Degree of Master
in Electronic and Telecommunications Engineering

Supervisors:

Msc André Ribeiro Lourenço
PhD Ana Luísa Nobre Fred

Jury:

President: PhD Mário Pereira Véstias

Vowels:

PhD João Pedro Barrigana Ramos da Costa
Msc André Ribeiro Lourenço
PhD Ana Luísa Nobre Fred

October 2013

Agradecimentos

As minhas primeiras palavras de agradecimento vão para André Lourenço e Hugo Silva pelas suas orientações, pela forma simples e compreensiva como as expunham, mesmo quando não as percebia pela primeira vez. À Prof. Ana Fred, pela sempre demonstrada confiança e liberdade, para poder pôr em prática todo o meu trabalho. Sem estas valiosas pessoas, este trabalho nunca seria possível.

Ao Prof. Raúl Martins pelos seus ensinamentos na área de Instrumentação Biomédica e pelo seu tempo despendido na resolução de dúvidas no inicio deste trabalho. Sem o seu precioso apoio este trabalho estaria incompleto.

Aos professores do Departamento de Electrónica e Telecomunicações e de Computadores (DEETC) pelo ensino e suporte educacional no decorrer da minha vida académica no Instituto Superior de Engenharia de Lisboa (ISEL), nomeadamente ao Professor João Costa pela introdução na área da Instrumentação Médica.

Gostaria de agradecer também o suporte financeiro dado pelo Instituto de Telecomunicações (IT-Lisboa) e pelo Institute for Systems and Technologies of Information, Control and Communication (INSTICC), no suporte da minha bolsa de investigação e materiais/equipamentos indispensáveis ao longo deste trabalho.

À Priscila Alves pela verdadeira amizade que foi crescendo ao longo deste último ano, pelos comentários e discussões construtivas que fizeram com que este trabalho ficasse completo.

Aos meus melhores amigos Tiago Venturinha e André Cigarro, pelo companheirismo e frontalidade. Têm sido fundamentais no meu crescimento enquanto Ser Humano.

Aos meus pais Manuel Soares Guerreiro e Maria Fernanda Francisco Guerreiro pelo suporte familiar que me têm dado ao longo destes 25 anos, dia após dia. À minha irmã, Cláudia Marina Francisco Guerreiro pelo seu constante apoio e encorajamento ao longo dos meus estudos.

Gostaria de agradecer também a Rita da Silva Luís, pelo suporte emocional e compreensão demonstrados nestes últimos 3 anos. A sua força tem-me mostrado que a vida é para ser vivida a dois.

As minhas últimas palavras de enorme reconhecimento vão para Gertrudes Vieira Martinho da Silva (Madrinha) e para o grande e meu mais que tudo José Joaquim dos Santos da Silva (Padrinho), pela forma como construiram os pilares da minha vida. Nunca os esquecerei!

Abstract

By definition, physical computing deals with the study and development of interactive systems that sense and react to the analog world. In an analogous way, physiological computing can be defined as the field, within physical computing, that deals with the study and development of systems that sense and react to the human body. While physical computing has seen significant advancements leveraged by the popular Arduino platform, no such equivalent can yet be found for physiological computing.

In this work we present "BITalino", a novel, low-cost, versatile platform, targeted at multimodal biosignal acquisition that can be used to support classroom activities, interface with other devices, or perform rapid prototyping of end-user applications in the field of physiological computing. BITalino integrates a micro-controller, a module for power conditioning and battery management, a wireless communication module that uses Bluetooth technology, allowing it to be connected to a computer, mobile phone or any other device that includes a Bluetooth receiver. Targeting the acquisition of physiological signals, it also integrates many specialized sensors to measure signals from the human body, in particular sensors to measure the activity of the heart, muscles, the activity of the sympathetic nervous system and movement. Additionally, it also includes a sensor that measures ambient light as well as a simple LED that gives easy feedback to the user. Besides as low-cost, another feature of the system is the fact that it is designed as a Lego, in which all the blocks described above can be detached from the main board, providing the user freedom to combine them in the manner that is most interesting for their own applications.

The emphasis of this work is on the main theoretical concepts of the Biosignals measurement, including Electrocardiography, Electromyography, Electrodermal Activity and Accelerometry, as well as detailed characterization of all hardware and firmware modules, including each block and their characterization tests and performance evaluation. We also present several examples of ap-

plications built using the developed platform to demonstrate its potential, namely: a Heartbeat-detector that uses Electrocardiographic (ECG) signals to trigger a LED; a light controlled by the wave of the hands, using Accelerometric (ACC) signals; a Muscle-controlled door lock, that uses Electromyographic (EMG) signals as a trigger; a didactic and interactive lie-detector setup that answers according to the emotional variations based on Electrodermal Activity (EDA) signals and Heart Rate (HR); and a twitting flower vase fitted with some additional non-BITalino sensors, that monitors the ambient light, soil moisture, relative humidity of air and temperature, to check the "health" status of a flower.

Keywords: Physiological Computing, Biosignal Acquisition, Electrocardiography, Electromiography, Electrodermal Activity, Accelerometry, Light sensing.

Resumo

O estudo e a utilização dos biosinais tem vindo a aumentar dentro da comunidade global de engenharia. Daí têm nascido novos campos de aplicações, para além das mais tradicionais em áreas da medicina. Enumerando alguns exemplos temos: monitorização da actividade humana em desporto, onde novos dispositivos (*Hardware e Software*) têm vindo a ser lançados pela indústria para auto-monitorização de performance; interação Homem-Máquina em jogos de computador/consola, possibilitando ao utilizador interagir com o jogo e vice-versa; em biometria, onde novos sistemas baseados em eletrocardiografia vêm adicionar novas propriedades de identificação às modalidades já existentes (reconhecimento facial, iris, impressão digital).

Adicionalmente, as recentes correntes de “Open-Source” e “Do-It-Yourself” têm vindo a transformar o modo como a indústria e o ensino de engenharia são executados. Desta forma, surgem novas plataformas de desenvolvimento, tais como o Arduino e o Raspberry Pi, que têm revelado uma vibrante comunidade de seguidores, e têm inspirado diversos projectos na área de sistemas embebidos. Contudo, muitos dos projectos encontrados no estado da arte focam-se principalmente na computação física, onde interagem com simples sensores e actuadores, tais como LEDs e botões ou mesmo pequenos motores, tendo poucos requisitos em termos de aquisição de sinal, nomeadamente baixa tolerância ao ruído e baixas frequências de amostragem, não sendo comparáveis com o estudo e aquisição de biosinais.

Com este trabalho apresentamos o "BITalino", uma versátil e multimodal plataforma para aquisição de biosinais, de baixo-custo, que pode ser utilizada como ferramenta em actividades de sala de aula, que possibilita a interacção com outros dispositivos, e que potencia a prototipagem rápida de aplicações finais de utilizador na área da computação fisiológica. O principal objectivo é tornar a aquisição de biosinais fácil e acessível a todos, desde estudantes, investigadores, engenheiros, e pessoas com interesse em trabalhar na área dos biosinais.

O BITalino é uma placa de hardware que integra um micro-controlador, um módulo de acondicionamento para a alimentação do sistema e controlo de carga da bateria, um módulo wireless para transmissão de dados utilizando a tecnologia Bluetooth, que possibilita a sua ligação a um computador, telemóvel, ou qualquer outro dispositivo que tenha um receptor Bluetooth. Integra também vários sensores muitos especializados na medição de sinais do corpo humano, nomeadamente, sensor para medir a actividade do coração, outro que permite medir a actividade muscular, outro para medir a actividade do sistema nervoso simpático e um outro que permite medir o movimento. Adicionalmente, integra também um sensor que permite medir a luz ambiente e também um simples LED que permite dar um feedback muito simples ao utilizador da placa. Além do baixo-custo, outra particularidade do sistema é o facto de estar desenhado como um Lego, em que todos os blocos descritos anteriormente podem ser destacados da placa principal, dando liberdade ao utilizador para combiná-los do modo que for mais interessante para a sua aplicação.

Neste trabalho são focados os principais conceitos teóricos para a medida de biosinais, nomeadamente Eletrocardiografia, Eletromiografia, actividade Eletrodérmica e Acelerometria, assim como a caracterização detalhada de todo o *hardware* e *firmware*, nomeadamente cada módulo e respectivos testes de caracterização e avaliação de performance.

Serão apresentados também alguns exemplos de aplicação construídos com base na plataforma desenvolvida, que demonstram o seu potencial, nomeadamente: um detector de ritmo cardíaco que utiliza sinais de eletrocardiografia para actuar num LED; um controlador de luz, que utiliza sinais de acelerometria para ligar ou desligar uma lâmpada; uma fechadura de porta que é controlada através de sinais de eletromiografia; um didático e interactivo detector de mentiras que se baseia nas variações emocionais captadas através dos sinais de actividade eletrodérmica e ritmo cardíaco; e uma flôr equipada com sensores adicionais que envia mensagens para o Twitter a informar o seu estado de saúde.

Palavras-chave: Computação Fisiológica, Aquisição de Biosinais, Eletrocardiografia, Eletromiografia, Atividade Eletrodérmica, Acelerometria, Sensor de Luz.

Contents

Contents	viii
List of Figures	xii
List of Tables	xiii
1 Introduction	1
1.1 Goals and Contributions	3
1.2 Document Organization	4
2 Concepts of Biosignals Measurement	5
2.1 Electrocardiography	5
2.2 Electromyography	8
2.3 Electrodermography	10
2.4 Accelerometry	12
2.5 The Electrode-Skin Interface - Impedance, Noise and DC Voltage	13
2.6 Interfering Input - External Noise Sources	18
2.7 Biopotential Amplifiers - Instrumentation Amplifier	20
3 BITalino - Architecture Description	25
3.1 Analog front-end	27
3.1.1 ECG and EMG	28
3.1.2 Electrodermal Activity	34
3.1.3 Accelerometry, Light sensing and LED actuator	36
3.2 Control, Power and Communication	38

3.3	Firmware	43
3.3.1	Real-time acquisition	46
4	Evaluation Tests	49
4.1	Qualitative tests.....	49
4.2	Quantitative tests	51
5	Applications	57
5.1	Beat-by-BIT	57
5.2	LockBIT and LightBIT	60
5.3	"Mentir de Verdade"	61
5.4	FlowerBIT.....	62
6	Conclusions and Future Work	63
	References	65

List of Figures

1.1 Examples of quality-of-life applications based on the biosignals. Redrawn and adapted from [1, 2, 3, 4], respectively.	2
1.2 DiY inspired devices.	3
2.1 Electrophysiology of the heart. The different waveforms for each of the specialized cells. Redrawn and adapted from [5].....	6
2.2 The Wilson central terminal (CT) is found at the center of the Einthoven triangle. Redrawn and adapted from [6].....	7
2.3 Precordial leads. Redrawn and adapted from [7].	8
2.4 Electrophysiology of the muscles. Redrawn and adapted from [8].....	9
2.5 Anatomical position of selected electrode locations. Redrawn and adapted from [9].	9
2.6 Electromyography electrodes placement. Redrawn and adapted from [8].....	10
2.7 Electrodermal Response (EDR) - Features used to describe the characteristics of a EDR includes the baseline (SCL) and amplitude of the SCR, the latency (between stimulus and SCR onset) and the recovery time. Redrawn and adapted from [10].....	11
2.8 Recommended electrode site on the fingers for the measurement of EDA.	12
2.9 Three orthogonal direction which accelerometer sensors can sense motion changes. Redrawn and adapted from [11, 12], respectively.	13
2.10 Electrode-electrolyte interface - The process of the metal oxidation occur. Redrawn and adapted from [13].....	14
2.11 Skin Anatomy, showing the various layers of the skin. Redrawn and adapted from [14].	14

2.12 Models of the electrode-skin impedance: a) simplified electrical model of the electrode-electrolyte interface; b) generalized model of the electrode-skin interface. Redrawn and adapted from [15].	15
2.13 Variation of the electrodes impedance with frequency. Redrawn and adapted from [13].....	16
2.14 Body surface biopotential electrodes (Ag-AgCl) often used in ECG and EMG acquiring apparatus. Redrawn and adapted from [13, 16], respectively.	17
2.15 Motion artefact in ECG acquired signal. Redrawn and adapted from [17].....	17
2.16 Coupling capacitances between the power line and lead wires causes parasite currents to flow through skin-electrode impedances. Redrawn and adapted from [18].	18
2.17 A common-mode voltage on the body is created by currents flow from the power line through the body to ground. Redrawn and adapted from [19].	19
2.18 Magnetic interference presented in Biopotential measurement. Redrawn and adapted from [19].	20
2.19 Differential vs common-mode input sources. Redrawn and adapted from [20]. . . .	21
2.20 The gain of the In-Amp is set by a single external resistor R_G . The value of R_G is selected according to $G = 1 + (\frac{100k\Omega}{R_G})$. Redrawn and adapted from the datasheet of INA333 [21].	22
2.21 The input buffers of an In-Amp circuit amplify the signal voltage while the common-mode voltage receives unity gain. However, the common-mode voltage is then rejected by the In-Amp's subtractor section. Redrawn and adapted from [20].	23
3.1 BITalino architecture overview.	25
3.2 All BITalino versions.	27
3.3 The In-Amp with AC coupling for DC suppression. Redrawn and adapted from the datasheet of AD8221.	28
3.4 A Sallen-Key circuit implementation - 4 th order low-pass filter cascading 2 stages of 2 nd order.	29
3.5 Diagram of the ECG sensor block (<i>Gain</i> = 1100; <i>Bandwidth</i> = 0.5 – 40 Hz) - An In-Amp with AC coupling to reject DC input voltages followed by a 4 th order lowpass Butterworth filter.	30
3.6 The schematic of the ECG circuit.....	30

3.7	ECG sensor - Frequency response (Gain = $60.83dB$ and Bandwidth = $0.5 - 40 Hz$).	31
3.8	Electrodes placement for ECG acquisition.	31
3.9	Diagram of the EMG sensor block (<i>Gain</i> = 1000; <i>Bandwidth</i> = $10 - 400 Hz$) - An In-Amp with AC coupling to reject DC input voltages followed by a 4^{th} order lowpass Butterworth filter.	32
3.10	The schematic of the EMG circuit.	32
3.11	EMG sensor - Frequency response(Gain = $60dB$ and Bandwidth = $10 - 400 Hz$).	33
3.12	Reference electrode placement in biosignals acquisition. Redrawn and adapted from [19].	33
3.13	Pinout of the ECG and EMG sensors.	34
3.14	Diagram of the EDA sensor block (<i>Gain</i> = 2; <i>Bandwidth</i> = $0 - 5 Hz$) - An OTA circuit followed by a 2^{nd} order lowpass Butterworth filter.	34
3.15	The schematic of the EDA circuit.	35
3.16	EDA sensor - Frequency response(Gain = $6.02dB$ and Bandwidth = $0 - 5 Hz$).	35
3.17	EDA block pinout	36
3.18	Schematics of the ACC, LUX and LED modules.	37
3.19	Pinout of the ACC, LUX and LED modules.	38
3.20	Hierarchical diagram of the MCU module. Redrawn and adapted from [22].	39
3.21	Control block pinout.	40
3.22	Power Supply Isolation between Analog and Digital circuits.	40
3.23	Voltage regulators included in the Power block. Redrawn and adapted from [23, 24, 25], respectively.	41
3.24	Power management circuit and battery. Redrawn and adapted from [26, 27], respectively.	41
3.25	Power block pinout.	42
3.26	Bluetooth block pinout.	43
3.27	State diagram of the firmware operation.	44
3.28	Modes and commands of the system operation.	44
3.29	A 4-bit LFSR with its state diagram. The XOR gates provide feedback to the registers that shift bits from left to right.	45
3.30	Data packet structure.	45
3.31	Synthesized waves related to the Simulated mode.	46
3.32	State diagram of the acquisition process.	47

4.1	SignalBIT application user interface.....	50
4.2	The frequency response of the ECG and EMG sensors.	54
4.3	Example of an ECG and an EMG signal acquired with the BITalino. ..	54
4.4	EDA sensor bandwidth characterization and signal example.	55
4.5	Example of an ACC and LUX signals acquired with the BITalino.	56
5.1	Beat-by-BIT device and ECG signal waveform.....	58
5.2	Algorithm flow diagram. Redrawn and adapted from [28].	58
5.3	Frequency response of the filters applied.	59
5.4	Signals obtained at each stage of the adopted algorithm. The signal in blue, x_n , represents the raw ECG signal, the signal y_n , in red, is the low-pass filtered ECG signal, the signal z_n , in green, shows the SSF signal, and finally in black we show the validated R peaks.	59
5.5	The individual components of the LockBIT/LightBIT application.	60
5.6	Screenshot of the "Mentir de Verdade" application. Adapted with permission from [29].....	61
5.7	FlowerBIT application.....	62

List of Tables

3.1	BITalino specifications.....	26
3.2	A summary of the physiological signals parameters.....	28
3.3	Sampling rate definitions.	46
4.1	Temporal uncertainty of the three versions of the BITalino (Board, Plugged and Freestyle).....	51
4.2	Dynamic specifications of the ADC (15 Hz sine wave; $F_s = 1k\ Hz$).....	53
4.3	Dynamic specifications (ECG and EMG, $F_s = 1k\ Hz$).	53
4.4	Overall information about power consumption of each BITalino block (approx. values).	56

1

Introduction

During the last century, biological signals were the basis of scientific advances on Biomedical Engineering and enabled several medical applications designed to aid in the diagnosis, monitoring or treatment of several medical conditions. Relevant examples include (but are not limited to): Electrocardiography (ECG) which interprets the electrical activity of the heart over a period of time, being detected by electrodes attached to the surface of the skin; Electroencephalography (EEG) which interprets the electrical activity of the brain by positioning electrodes along the scalp; Electromyography (EMG) which interprets the electrical activity produced by skeletal muscles, normally being detected by electrodes attached to the surface of the skin; Electrodermography (EDA) which refers to electrical changes measured at the surface of the skin that arise when the skin (sweat glands) receives innervating signals from the brain, essentially measuring the electrical conductance between 2 points of the skin surface; among many other applications (e.g. Skin Temperature (SKT), Respiratory Volume (RV), Blood Volume Pulse (BVP), Oximetry (SpO₂), etc.).

The modern uses of biosignals have become an increasingly important topic of study within the global engineering community (in areas including computer science, informatics, electrical engineering, among others) and consequently, much evidence shows that the biosignals are clearly a growing field of interest. In Figure 1.1a) a heart-rate monitor is shown, as an example of human enhancement applications on fitness, enabling the self-monitoring/ self-sensing, and optimization of body performance, which is being taken seriously by global industrial engineering landscape, that are launching new devices and software [30]. In Figures 1.1b) and c) are shown two recent applications of the biosignals within Human-Computer Interaction (HCI), on gaming and entertainment, which enables people to interact with the machine and vice versa [31, 32, 3].

More recently in biometric systems, a particular kind of biosignal (ECG - Figure 1.1d) is being used due to its desirable proprieties, when compared to other modalities (iris, face, fingerprint). It is continuously available and can only be collected in live subjects, it can be easily acquired and provide information which is directly related to the psychophysiological condition of the subject because it is influenced by the sympathetic and parasympathetic nervous system [33, 34]. Moreover, the biosignals are also being used in many other disciplines, such as, biofeedback [35], biomechanics [36], and telemedicine [37].

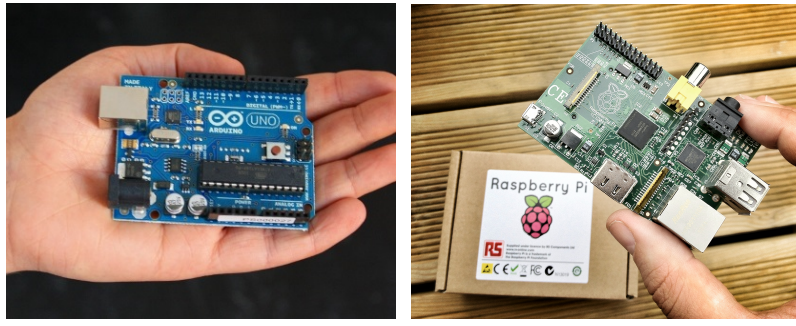


Fig. 1.1. Examples of quality-of-life applications based on the biosignals. Redrawn and adapted from [1, 2, 3, 4], respectively.

The more recent currents of "Open-Source" play a transforming role on several aspects by global engineering. In addition, some projects are being inspired by results found within the "Do-It-Yourself" (DiY) communities, as shown by the several projects that have reached remark-

able achievements in shaping educational curricula at a global scale. The most broadly known examples are based on the Arduino platform [38, 39, 40, 41], which is an open-source electronics prototyping environment providing an easy-to-use hardware and software to anyone (Figure 1.2 a)). Many Arduino variants are appearing, showing a vibrant community of followers. The Lily-pad arduino is an example, designed for wearable computing (in particular, e-textiles) [42, 43].

Another notable example is the Raspberry Pi platform [44], which is a credit-card sized computer with the computational power of a small PC (Figure 1.2 b)). It was designed to be cheap, accessible and low-cost, which provides an easy environment for prototyping as well. Today, it is also revolutionizing the way in which embedded systems are seen and taught worldwide.



(a) Arduino. (b) Raspberry Pi.

Fig. 1.2. DiY inspired devices.

However, most of the projects found in the state-of-the-art are targeting areas such as physical computing and robotics, that is, generally they only interface with simple sensors and actuators such as switches, LEDs or even small motors. Also, they are not able to adequately deal in full with the requirements in terms of body signal acquisition. Whether due to low tolerance to noise, low sampling rates, crosstalk between sensor inputs, size or performance issues.

1.1 Goals and Contributions

In this thesis we propose a novel, versatile and low-cost wireless platform entitled "BITalino", which consists of an hardware device slightly bigger than a "Credit Card" form factor, that integrates multiple measurement sensors for biosignal data acquisition. It can be used to support physiological computing applications or even to support classroom activities, interfacing with other devices or performing rapid prototyping of end-user applications, which ensures a non-

invasive apparatus and provides an easy acquiring of the biosignals. The goal is to make the biosignals readily available and accessible for everyone, allowing students, researchers, hobbyists and other people, with interest in starting to work in the field of the biosignals, to interact and have easy access to their own body signals.

During the realization of this thesis several articles were submitted:

- BITalino: A Multimodal Platform for Physiological Computing (presented in ICINCO 2013), as author;
- Performance Comparison of Low-Cost Hardware Platforms Targeting Physiological Computing Applications (accepted in CETC 2013) as author;
- A Novel Hardware Framework for Physiological Computing (accepted in PhyCS 2014) as co-author.

1.2 Document Organization

The remainder of this document is organized as follows:

- Chapter 2 describes the theoretical concepts that form the basis of this work. The emphasis is on the understanding of the biological processes that are the origin of the signals that are to be acquired by the BITalino platform;
- Chapter 3 describes the BITalino architecture, which includes hardware and firmware characterization and design details;
- Chapter 4 describes the tests used to evaluate the device, such as, performance and dynamic specifications of each block within the BITalino;
- Chapter 5 describes some applications where the BITalino fits, showing the potential of the developed platform;
- Chapter 6 finalizes the document with the conclusions and future work.

Concepts of Biosignals Measurement

Biosignals can be commonly defined as observations of electrophysiological, biomechanical, or chemical processes of a living organism, ranging from protein and gene sequences, neural or cardiac rhythms, to tissue and organ images [45].

Certain systems/components of the body such as, nervous, muscular, or glandular tissue, create their own bioelectric potentials - called Biopotentials. Biopotentials are produced as a result of electrochemical activity of a certain class of cells, known as excitable cells which are associated with the conduction along the sensory and motor nervous system, muscular contractions, brain activity, heart contractions, etc [45]. On the other hand, biomechanics is the study of the function of the biological systems by means of the mechanical principles of living organisms, particularly their movement and structure within widespread subfields such as, body dynamics, kinetics, physiology, gait analysis, ergonomics, etc [46]. In this work, the main emphases is on biopotentials (ECG, EMG and EDA) and biomechanical (Accelerometry) signals. In the following Sections we detail the principles behind them.

2.1 Electrocardiography

The heart is composed of a cardiac muscle, called myocardium [5]. It consists of four compartments: the right and left atria and ventricles. Its main function is to pump blood to the systemic and pulmonary circulation. More deeply, the heart generates electrical current, by the contraction of its muscle cells. These cells have the capability of self-stimulation, which generates the cardiac rhythm, normally a regular sequence of heart beats.

As illustrated in Figure 2.1, the cardiac cycle is normally initiated by the sinoatrial node (SA node) and followed by the atrioventricular node (AV node). The SA nodal cells are self-excitatory,

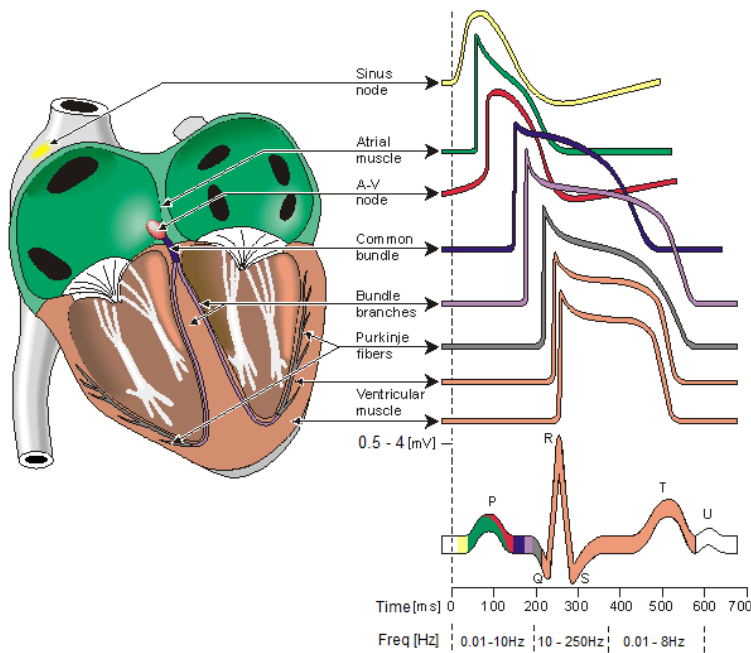


Fig. 2.1. Electrophysiology of the heart. The different waveforms for each of the specialized cells. Redrawn and adapted from [5].

pacemaker cells. They generate an action potential at the rate of about 70 per minute. Between them, the internodal atrial connects the SA and AV nodes, and regulate the passage of the cardiac impulse from the atria to the ventricles. This action is composed of a common bundle, called the bundle of His (named after German physician Wilhelm His, Jr., 1863-1934) [5]. This system enables the electrical triggering impulses generated at the SA node, to be propagated from the wall of the right atrium (where the SA node is located), to the deeper tissues of the ventricular muscles (through where the Purkinje fibers are spread). From the inner side of the ventricular wall, the many activation sites cause the formation of a wavefront, which propagates through the ventricular mass toward the outer wall. This process results from cell-to-cell activation. After each ventricular muscle region has depolarized, repolarization occurs. The termination of activity appears as if it were propagating from epicardium (the outer side of the cardiac muscle) toward the endocardium (the inner side of the cardiac muscle) [5].

The typical ECG waveform is characterized by P-QRS-T-U complexes (see Figure 2.1). Each complex has a particular spectral content: P wave, with a duration of approximately 150 ms, and spectral content up to 10 Hz; the QRS complex has a relatively higher amplitude compared with the other waves, with a duration of approximately 100 ms in a normal heartbeat, and has

mostly frequencies between 10 to 250 Hz; the T wave, with a duration of approximately 300 ms, and spectral content up to 8 Hz and is mostly dependent on the heart rate [34].

The first ECG recording device was developed by Willem Einthoven, in his pioneer work [6], where he published a description of the first clinically ECG measuring system, in 1908. The "Einthoven's triangle", named in his honour, refers to the imaginary inverted equilateral triangle centered on the chest and the points being the standard leads on the arms and leg.

Later, Frank Norman Wilson proposed a new method where Electrocardiographic unipolar potentials can be defined. He suggested the use of the central terminal as reference, and this idea is being used until the present days [6]. The unipolar potentials result from the connection of a resistor from each terminal of the limb leads to a common point, the central terminal (CT), as shown in Figure 2.2. That unipolar potentials should be measured with respect to this terminal. So, the Wilson central terminal represents the average of the limb potentials, because the total current into the central terminal from the limb leads must add to zero to satisfy the conservation of current (Kirchhoff's 1st Law) describe that the algebraic sum of currents in a network of conductors meeting at a point is zero ($I_R + I_L + I_F = 0$)[6].

The resistance value of each terminal has significant importance and, gratefully, nowadays the input impedance of the biopotential amplifiers (Instrumentation Amplifiers) is high, which increases the Common-mode Rejection, as will be described in Sections 2.5 and 2.7. In Figure 2.2 is also illustrated, within the Einthoven triangle, the bipolar limb leads which are usually designated as I, II and III and they track the electrical potential of the heart when three electrodes are attached at the right and left hand and left foot.

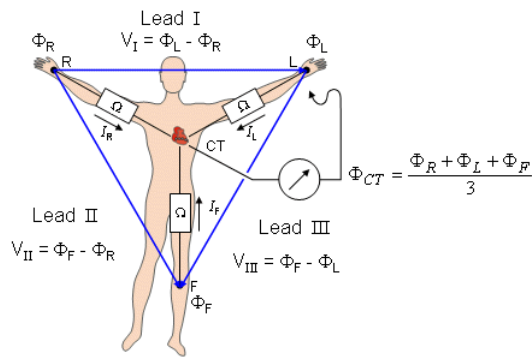


Fig. 2.2. The Wilson central terminal (CT) is found at the center of the Einthoven triangle. Redrawn and adapted from [6].

The voltages and potentials represented are:

- V_I = the voltage of Lead I;
- V_{II} = the voltage of Lead II;
- V_{III} = the voltage of Lead III;
- Φ_L = potential at the left hand;
- Φ_R = potential at the right hand;
- Φ_F = potential at the left foot.

Another category of lead orientation is the precordial leads ($V_1, V_2, V_3, V_4, V_5, V_6$) which are recorded with 6 additional electrodes attached to the chest and give more information within the electrocardiogram, as illustrated in Figure 2.3.

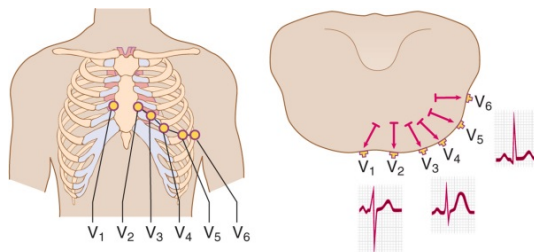


Fig. 2.3. Precordial leads. Redrawn and adapted from [7].

In spite of the physiology of the ECG, the signal is regulated by the sympathetic nervous system and its variation make the ECG signal directly susceptible to emotional states. In addition, the artefacts introduced by the electrode-skin interface, motion and the potential induced on the surrounding area by the power line cables make the electronic measurement system a critical issue. All these points will be further described in Sections 2.5, 2.6 and 2.7.

2.2 Electromyography

The electromyographic signal (EMG) is the electrical manifestation of the neuromuscular activation associated with a contracting muscle. As illustrated in Figure 2.4, when a muscle is activated by the Central Nervous System (CNS) through the motor neuron (which controls the body movements as well as most functions of the body and mind), muscle fiber contraction takes place, following the depolarization of the outer muscle-fiber membrane. The depolarized zones

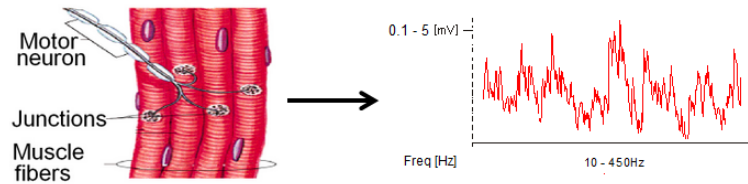


Fig. 2.4. Electrophysiology of the muscles. Redrawn and adapted from [8].

of the fibers of each recruited Motor Unit (MU) creates an electrical field and generates voltage contributions that add up on the skin to form a voltage distribution [47].

This sum is weighted by the distance of each source from the skin. By placing electrodes over the skin, the voltage in those points (surround area) covered by the electrode can be measured. Typically, two electrodes per muscle are used (Figure 2.5) and the difference between the two cutaneous potentials is acquired [48].

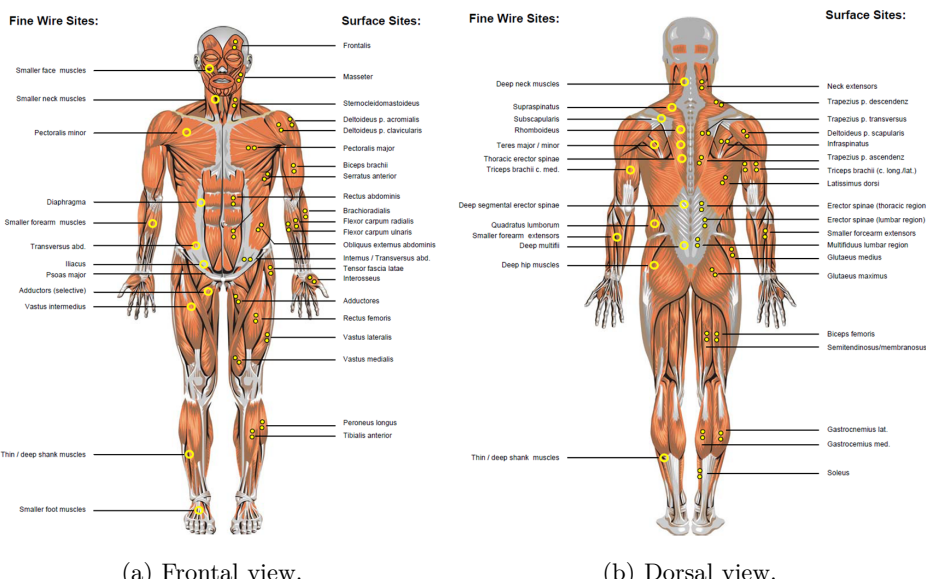


Fig. 2.5. Anatomical position of selected electrode locations. Redrawn and adapted from [9].

The Electromyographic signal on focus in this work is surface Electromyography (sEMG), detected by means of a couple of electrodes. sEMG is a measure of the electrical potential present over the skin surface in consequence of a muscle contraction, as illustrated in Figure 2.6. The typical sEMG waveform is characterized with a spectral content between 10 to 450 Hz with amplitude up to 5 mV, dependent on the particular muscle [48].

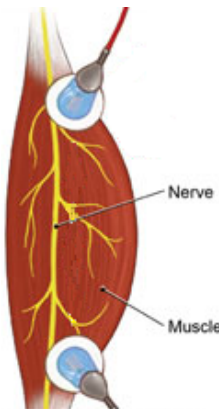


Fig. 2.6. Electromyography electrodes placement. Redrawn and adapted from [8].

If surface electrodes are placed on the skin parallel to the muscle fibers, then the travelling potential is detected by the electrodes with a temporal delay that depends on the muscle fiber conduction velocity. Similar to the ECG, the EMG signal is also recorded with electrodes connected to an electronic device which provides a bipolar voltage measurement between them (Instrumentation Amplifier). As described in Section 2.7, the differential detection technique has many advantages, namely, attenuating potentials that are equal under the both electrodes (Common-Mode Voltage), such as signals coming from far muscles with interposed tissues into the electrodes area, and the potential induced by the electrical field produced by the power line cables, as already focused in Section 2.1 and which will be deeply described in Section 2.6

2.3 Electrodermography

In previous Sections 2.1 and 2.2, the focus was on the need to consider the skin-electrode interaction to record the surface potential non-invasively. In this Section we focus on the skin response itself, and will characterize its associated signals.

The Electrodermal Activity (EDA) refers to all electrical phenomena in skin, and it changes measured at the surface due to the variation of the perspiration. This is associated with sweat gland activity, and it is regulated by the Sympathetic Nervous System, which is directly related to emotional variations and can be a good indicator of arousal (suitable in psychophysiology applications). The Sympathetic Nervous System is part of the Autonomic Nervous System, and is responsible for the control of visceral functions such as heart rate, digestion, respiration, and perspiration. The majority of these functions operate on an unconscious level and take over for

the auto-pilot of each subject. As the body comes under stress, sweat production increases, and the sweat ducts fill. Sweat is a weak electrolyte and a good conductor. Increased sweat production creates several low resistance pathways across the surface of the skin. A relaxed subject with drier skin will have a higher electrical resistance, while a subject under stress will produce more sweat, having a lower electrical resistance in the skin.

The Electrodermal Response(EDR) is one of the Electrodermal measurements available (including SCL - Skin Conductance Level; SCR - Skin Conductance Response; etc.). The variable that is measured is skin conductance, expressed in Siemens (S), or its reciprocal, skin resistance which is expressed in $[Ω]$, as described in Equation 2.1 (G is the skin conductance and R is the electrical resistance associated).

$$G[\mu S] = \frac{1}{R[k\Omega]} \quad (2.1)$$

As illustrated in Figure 2.7, there are two types of skin conductance that can be characterized: Tonic skin conductance, which is the baseline level of the skin conductance, and is generally referred to as Skin Conductance Level (SCL); and Phasic skin conductance, which is the type that changes when events take place with a frequency range of $0.05 – 1 Hz$. Although, each subject has its own particular SCL, with a typical tonic frequency range of $0 – 0.05 Hz$, and it can vary over time according to the user psychological state and autonomic regulation. Environment stimuli such as, sights, sounds or arousal, will evoke time related changes in sweat glands activity and consequently in skin conductance [49]. The typical range of spontaneous EDRs is often between $0.002 – 1 \mu S$ and/or $1 – 500 k\Omega$ [50].

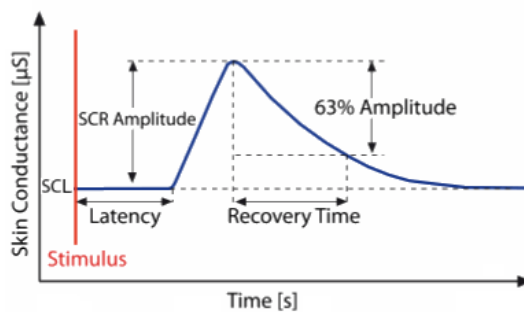


Fig. 2.7. Electrodermal Response (EDR) - Features used to describe the characteristics of a EDR includes the baseline (SCL) and amplitude of the SCR, the latency (between stimulus and SCR onset) and the recovery time. Redrawn and adapted from [10].

The EDA is usually measured at the palmar sites of the hands or the feet where the density of sweat glands is highest ($> 2000/cm^2$), such as the example shown in Figure 2.8, following a proposal by Venables and Christie (1980) [49]. As will be seen in Chapter 3, the electronics associated with the measurement of EDA can be called as Transconductance Amplifier (OTA).

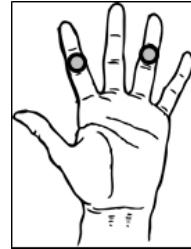


Fig. 2.8. Recommended electrode site on the fingers for the measurement of EDA.

2.4 Accelerometry

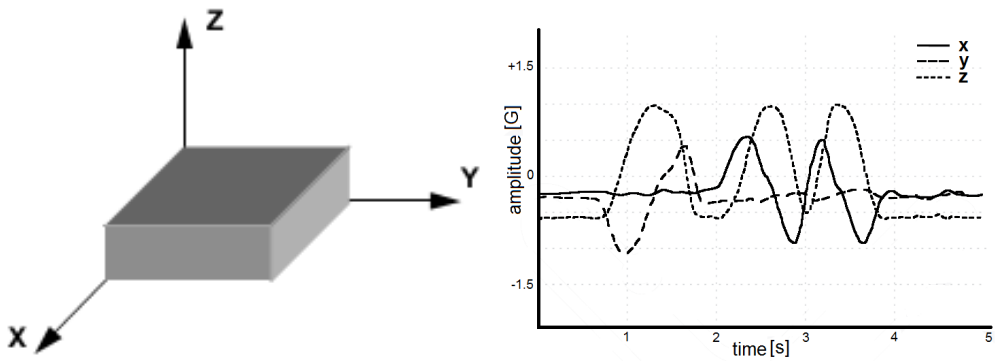
Acceleration is defined as the rate of change of velocity with respect to time. Mathematically, acceleration is determined by taking the derivative of the velocity as a function of time, as described in Equation 2.2 [51].

$$a = \lim_{\Delta t \rightarrow 0} \frac{\Delta v}{\Delta t} = \frac{dv}{dt} \quad (2.2)$$

Acceleration measurements are a particular topic in research applications and studies of biomechanic analysis which are widely spread in areas such as, sports in order to obtain a greater understanding of athletics performance and to reduce sport injuries [52], healthcare as a method of rehabilitation and gait analysis [11] and even in entertainment (mobile phones tilt and motion sense in gaming consoles)[53, 54].

Mechanic forces are divided into two main categories: Dynamics, which are due to external forces (systems in motion when acceleration is present); and Statics, which refers to gravity force (systems that are in a state of constant velocity even at rest - with no motion)[46].

Technological advancements in Micro Electronic Mechanical Systems (MEMS) technology, have led to the development of MEMS accelerometer sensors in recent years. This has made it possible to design several applications based on body motion, which operates on the principles of detecting changes on body positioning, by tracking acceleration changes in three orthogonal directions [11], as illustrated in Figure 2.9a).



(a) 3-axis Accelerometer sensor.

(b) 3-axis Accelerometer signal example.

Fig. 2.9. Three orthogonal direction which accelerometer sensors can sense motion changes. Redrawn and adapted from [11, 12], respectively.

MEMS is a semiconductor technology that builds micromechanical structures and electrical circuits into a single silicon chip. The MEMS accelerometer is a sensor based on this technology to achieve acceleration sensing on single-axis, dual-axis, or tri-axis conditions. Depending on the application, the accelerometer may offer different ranges of detection from several G to tens of G of digital or analog output.

The typical Accelerometer waveforms (associated with the human body motion) are characterized with a spectral content up to 10 Hz and ranging $\pm 1.5 G$, depending on the particular body movement [55], as illustrated in Figure 2.9b)

2.5 The Electrode-Skin Interface - Impedance, Noise and DC Voltage

In order to measure potentials and, thus, currents in the body, it is necessary to provide some interface between the body and the electronic measuring circuit. Biopotential electrodes carry out the transducer function and thus it converts biological information into a measurable and quantifiable electrical signal. It converts one form of energy into another.

For the passage of current from the body to an electrode, and consequently, into an electronic circuit, it is required a charge transfer called the electrode-electrolyte interface. The electrolyte represents either the body fluid containing ions (sweat) or an electrolyte solution (gel material) applied between the electrode and the skin. The electrode-electrolyte interface occurs when a metal is placed or linked with an electrolyte solution, and an ion-electron exchange happens - a current crosses the interface, passing from the electrode to the electrolyte. This means that

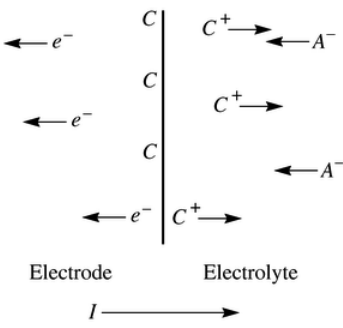


Fig. 2.10. Electrode-electrolyte interface - The process of the metal oxidation occur. Redrawn and adapted from [13].

the electrons are moving in an opposite direction of the current in the electrode, the cations are moving in the same direction as the current, and the anions are moving in an opposite direction of the current in the electrolyte. A potential E_{hc} called the half-cell potential is generated as a result of the charge layer and it is measured with respect to another electrode [56, 13]. This process is called oxidation of the metal that is illustrated in Figure 2.10.

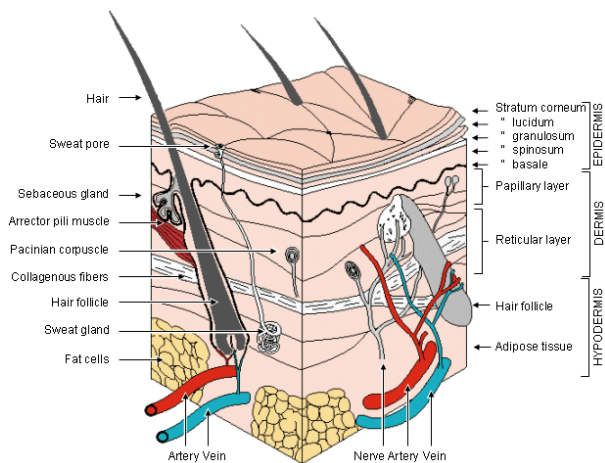


Fig. 2.11. Skin Anatomy, showing the various layers of the skin. Redrawn and adapted from [14].

The interpretation of the skin conductance requires some understanding about the structure of the tissues at and under the skin surface. The skin anatomy can be visualised in Figure 2.11. The skin consists of three principal layers: hypodermis, which is the deepest one, dermis and epidermis, at the surface. These layers are covering the body to protect it from its environment.

The deeper layers of the skin contains blood vessels, nerves, sweat glands and hair follicles. The uppermost layer, the epidermis, is composed of dead cells (statum corneum) on the surface of the skin and thus, it has a high impedance [14].

The properties and the behaviour of the electrode-skin impedance have already been addressed in other research work [15], where they deal with the use of surface electrodes in biopotential recordings. The characteristics of the electrodes are sensitive to the current passing through them, and can be modelled by a non-linear RC circuit whose components are frequency and current dependent [13]. The electrode-electrolyte interface is commonly described by the models shown in Figure 2.12.

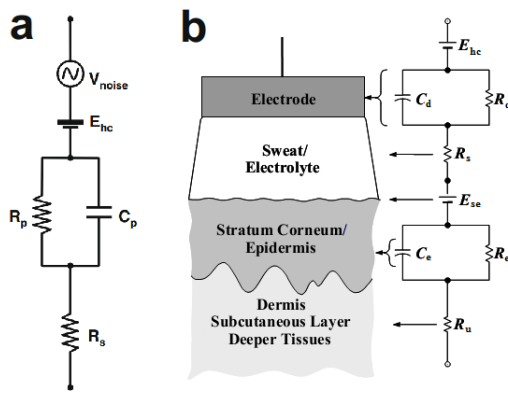


Fig. 2.12. Models of the electrode-skin impedance: a) simplified electrical model of the electrode-electrolyte interface; b) generalized model of the electrode-skin interface. Redrawn and adapted from [15].

Analysing the circuit shown in Figure 2.12a, where E_{hc} is the half-cell potential, R_p and C_p represent the impedance associated with the electrode-electrolyte interface and R_s is the resistance due to the interface effects, and it is evident that the electrode impedance is frequency dependent. At high frequencies, where $1/\omega C \ll R_p$, the impedance is constant at R_s . At low frequencies, where $1/\omega C \gg R_p$, the impedance is also constant at $R_s + R_p$. At frequencies between these values, the electrode impedance is frequency dependent as illustrated in Figure 2.13 [56, 13].

When an electrode is coupled to the skin, the skin surface can be considered as a semi-permeable membrane and thus, a potential difference E_{se} exists across the skin. A model for an electrode attached to the skin surface is shown in Figure 2.12b. The resistance R_s is associated

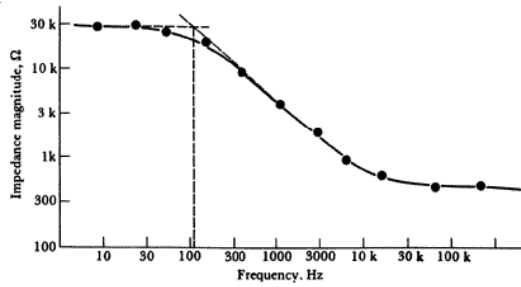


Fig. 2.13. Variation of the electrodes impedance with frequency. Redrawn and adapted from [13].

with the interface effects of the electrolyte between the electrode and the skin. The epidermal layer has an electric impedance associated that behaves as a parallel RC circuit, and thus is frequency dependent. The dermis and the deepest layers are, in general, pure resistances (R_u) and generate insignificant DC potentials [13].

Another important issue is the noise level of the electrode. Noise intrinsically associated with the metal-electrolyte interface is always present. At frequencies above 100 Hz, the electrode noise is equal to the thermal noise generated by the electrode-skin resistance, but at low frequencies ($f < 100 \text{ Hz}$) the noise of the skin-electrode interface is significantly higher with respect to the thermal noise [57, 58]. Spectral characteristics of the electrode–skin noise showed a 1/f behaviour for very low frequencies ($f < 30 \text{ Hz}$), but at higher frequencies the noise added by the amplifier circuit is dominant [59]. In general, silver/silver chloride (Ag-AgCl) electrodes present the lowest noise interface and are recommended for biopotentials recording [60]. There are some properties that make it a good choice for an electrode. Firstly, it is a kind of non-polarized electrode, which means that current flows freely across the electrode junction. Secondly, it does not produce so much noise between them. Potential fluctuations may exist between the electrodes and it can generate noise; however with the Ag-AgCl electrodes this noise can be reduced because the AgCl layer has a stabilization function [56].

In addition, the level of the electrode–skin noise is significantly dependent on the skin treatment [59]; if the skin impedance is very high, it can be a problem, since it is difficult for the potentials generated by the biosignals to cross this barrier and the signal amplitude will be low. Consequently, it would be important to reduce or short-circuit the skin impedance. However, skin impedance can be reduced by cleaning the skin surface and thus removing the stratum of dead cells. Using an electrolyte solution (gel material) applied between the electrode and the skin is also suitable [56]. Contact impedance may range from a few $k\Omega$ to a few $M\Omega$, depending

on the electrode size and the skin condition. In Figure 2.14 is shown the silver/silver chloride (Ag-AgCl) electrode which is often used in biopotential applications.

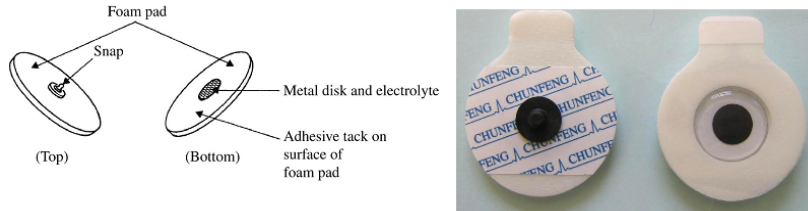


Fig. 2.14. Body surface biopotential electrodes (Ag-AgCl) often used in ECG and EMG acquiring apparatus. Redrawn and adapted from [13, 16], respectively.

Another consequence of the electrode-skin interface is the offset DC voltage. When the electrodes are attached to the skin in different contact points, a few hundred mV are generated due to the impedance values associated with each electrode-skin interface. Gratefully, nowadays there are front-end amplifiers that can reduce this undesired offset.

When the electrode is moved with respect to the electrolyte (mechanical alteration of the electrode-electrolyte interface), this movement cause a momentary change of the half-cell potential and thus a potential difference appears between the two electrodes during this movement. This momentary potential is known as motion artefact and can be a serious problem of interference in the measurement of biopotentials, as illustrated in Figure 2.15. Observation of this matter reveals that a major component of this noise is at low frequencies. Thus, motion artefacts can be the most difficult type of noise to cancel. In particular, when the spectrum of motion artefact completely overlaps with the desire signal.

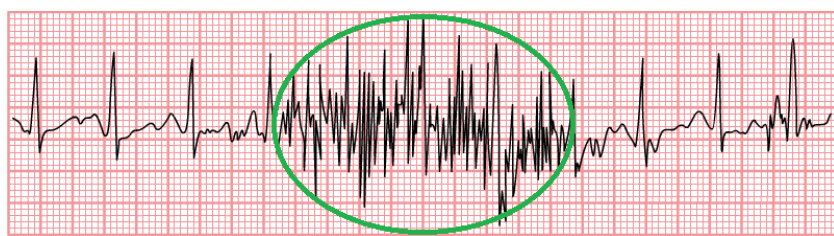


Fig. 2.15. Motion artefact in ECG acquired signal. Redrawn and adapted from [17].

2.6 Interfering Input - External Noise Sources

The aim of an instrumentation circuit is to isolate the desired inputs. However there are some quantities of undesired inputs, called interfering inputs, that affect the instrumentation as a consequence of the principles of acquisition.

In biopotential applications such as the example represented in Figure 2.16, the high frequency signals from radio frequency (RF) and the signal components from electric power lines are undesired sources of noise. These components are added with the desired signal and appear at the input of the biopotential amplifier. These, cause displacement currents which flows to electrodes and create a differential voltage between the impedances of electrode-skin interface as well as the impedance of the user body [50].

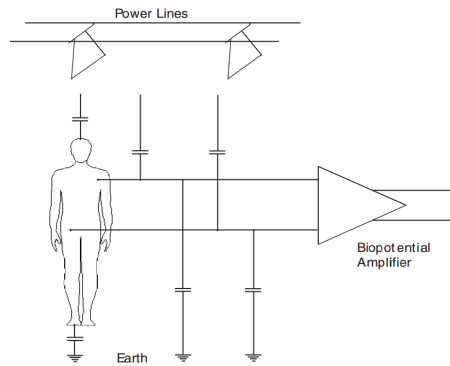


Fig. 2.16. Coupling capacitances between the power line and lead wires causes parasite currents to flow through skin-electrode impedances. Redrawn and adapted from [18].

In fact, the signal from power lines would be the main source of external interference (noise) in biopotential measurements. Power lines are connected to equipments and appliances everywhere, mainly inside the floor and walls.

Equations 2.3, 2.4, 2.5, 2.6 and 2.7 describe how this noise is injected and affects the biosignals acquisition, and in Figure 2.17 can be visualised a scenario occurring when the current flows from the power lines through the body and generate a common-voltage v_{cm} called common-mode voltage. The v_{cm} is defined by the Equation 2.3, where i is the current generated by the electromagnetic field from the power lines, and Z_G is the impedance between the human body and the Ground.

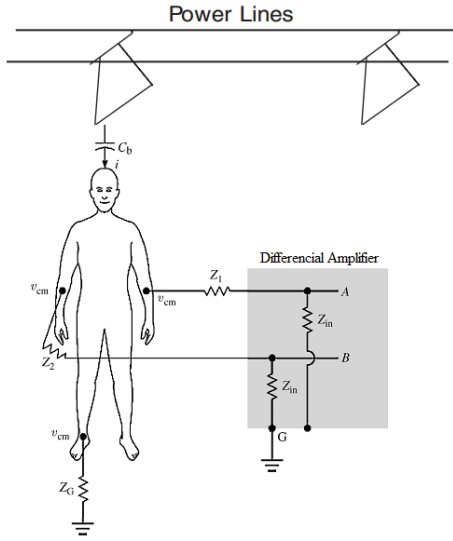


Fig. 2.17. A common-mode voltage on the body is created by currents flow from the power line through the body to ground. Redrawn and adapted from [19].

$$v_{cm} = i \times Z_G \quad (2.3)$$

Substituting the Equation 2.3 for the typical values [19], we have:

$$v_{cm} = (1\mu A)(100k\Omega) = 100mV \quad (2.4)$$

In poor electrical environments in which $i > 1\mu A$, v_{cm} can be greater than $100mV$. For ideal Amplifiers this would not cause any problem, because they can perfectly reject the common-mode voltage ($Z_{in} = \infty$). However, real Amplifiers have finite input impedance Z_{in} and this factor should be taken into account. Thus, v_{cm} will be affected by the attenuator action of the skin-electrode impedances (Z_1 and Z_2) and Z_{in} . Calculating again the noise level from this source, we obtain:

$$v_A - v_B = v_{cm} \left(\frac{Z_2}{Z_{in} + Z_2} - \frac{Z_1}{Z_{in} + Z_1} \right) \quad (2.5)$$

Since Z_{in} is much higher than Z_1 and Z_2 ,

$$v_A - v_B = v_{cm} \left(\frac{Z_2 - Z_1}{Z_{in}} \right) \quad (2.6)$$

Substituting with reference values, we obtain:

$$v_{cm} = (100mV) \left(\frac{20k\Omega}{100M\Omega} \right) = 200\mu V \quad (2.7)$$

As described by the Equations 2.4 and 2.7, the v_{cm} can be reduced from $100mV$ to $200\mu V$, if we minimize the skin-electrode impedances and provide a high biopotential amplifier input

impedance Z_{in} . Some v_{cm} is always present, so it is a critical factor to provide biopotential amplifiers with high Common-Mode Rejection Ratio (CMRR), since the aim is to minimize the impact of this undesired voltage. The following Section 2.7 provides a particular discussion of this important issue.

Another source of interference is a magnetic induction from power lines. If such magnetic field pass through the effective single-turn coil produced by the biopotential circuit, lead wires, and the user, an induced voltage is presented in this loop, as illustrated in Figure 2.18a. However it can be reduced by twisting the lead wires together and keeping them close to the body, as illustrated in Figure 2.18b.

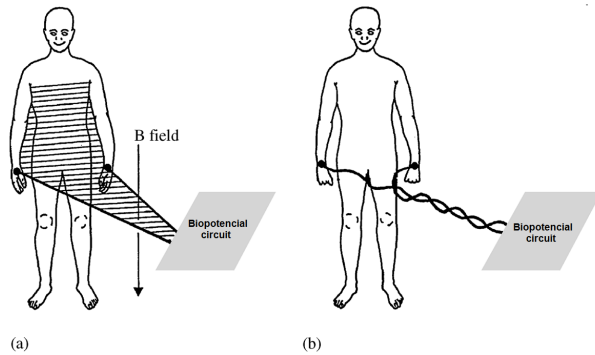


Fig. 2.18. Magnetic interference presented in Biopotential measurement. Redrawn and adapted from [19].

2.7 Biopotential Amplifiers - Instrumentation Amplifier

In general, signals from physiological activity have very small amplitudes and should be amplified and filtered before their recording and processing. So, as focused in the previous Section, in order to measure biopotentials, it is essential to provide an electronic measuring circuit. Therefore, a biopotential amplifier is necessary in order to increase the amplitude of the weak potential differences generated from the biological electric signals. An Instrumentation Amplifier (In-Amp) is widely used as a biopotential amplifier, because it has some characteristics that make it ideal for measuring signals from low level output transducers in noisy environments. The In-Amp is a device that amplifies the difference between two input signal voltages while rejecting any signals that are common to both input terminals. In fact, Common-Mode Rejection (CMR) is

the most important function that an In-Amp provides, because it is the property of cancelling out any signals that are common on both input terminals, while amplifying any signals that are differential between the inputs. Both DC and AC Common-Mode Rejection are important, since inadequate CMR of undesired sources (such as, offset DC voltage generated by the contact features of the electrode-skin interface and electric power lines signal) cause errors and, therefore, is difficult to remove afterwards. Fortunately, most modern IC In-Amps provide excellent DC and AC common-mode rejection. Figure 2.19 provides a functional block diagram of an In-Amp with the undesired common-mode voltage.

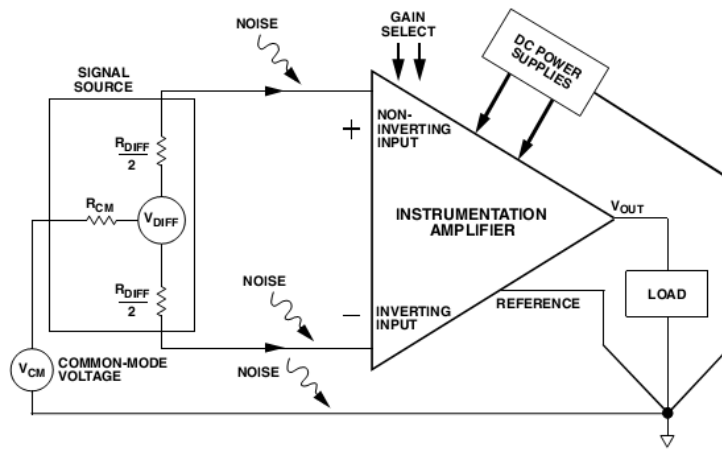


Fig. 2.19. Differential vs common-mode input sources. Redrawn and adapted from [20].

Mathematically, common-mode rejection can be represented as

$$CMRR = A_D \left(\frac{V_{CM}}{V_{OUT}} \right) \quad (2.8)$$

where:

- A_D is the differential gain of the amplifier;
- V_{CM} is the common-mode voltage present at the amplifier inputs;
- V_{OUT} is the output voltage present when a common-mode input signal is applied to the amplifier;

Usually, the CMRR is expressed in terms of a logarithmic expression of CMR. That is, $CMR = 20 \log_{10} CMRR$. Modern IC In-Amps with decent qualities can provide good CMR values, that is, values between $80dB$ to $120dB$.

As it is exposed in Section 2.6 and in order to reduced the common-mode voltage, it is fundamental to provide a high input impedance to increase the CMR factor. An In-Amp is a differential amplifier which is designed with input buffer amplifiers. So, the impedances of the input sources will have a minimal effect on the circuit's common-mode rejection and the use of a dual Op-Amp for two input buffer amplifiers is preferred because they will better track each other over temperature changes and save board space as well. The circuit of Figure 2.20 provides a clear illustration of the most popular configuration for In-Amp design and the Equation 2.9 describes its transfer function.

$$V_O = G \times (V_{IN+} - V_{IN-}) + V_{REF} \quad (2.9)$$

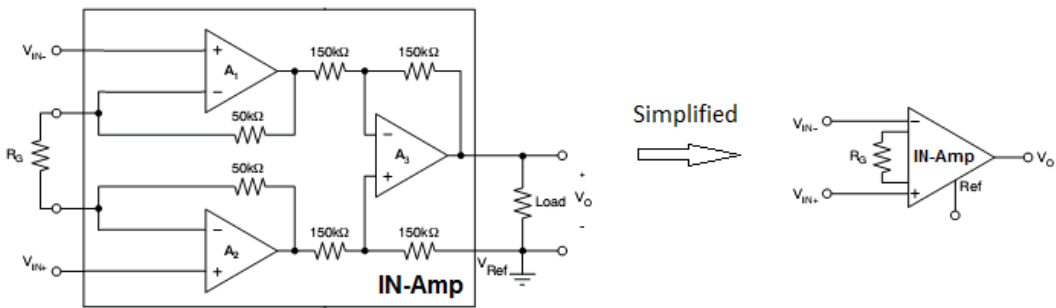


Fig. 2.20. The gain of the In-Amp is set by a single external resistor R_G . The value of R_G is selected according to $G = 1 + (\frac{100k\Omega}{R_G})$. Redrawn and adapted from the datasheet of INA333 [21].

The Figure 2.21 together with the Equations 2.10, 2.11 and 2.12 help to explain how common-mode voltage is being reduced.

The input amplifiers (A₁ and A₂), are operating at a gain of 1000, while the output amplifier is providing unity gain. This means that the voltage at the output of each input amplifier will equal one-half of the input voltage $\times 1000$, plus any common-mode voltage that is present on the inputs. Therefore, if a 10mV differential signal is applied to the amplifier inputs, amplifier A₁'s output will equal +5V, plus the common-mode voltage, and A₂'s output will be -5V, plus the common-mode voltage.

$$V_{OUT_{A1}} = (10mV \times 500) + CMV = 5V + CMV \quad (2.10)$$

$$V_{OUT_{A2}} = -(10mV \times 500) + CMV = -5V + CMV \quad (2.11)$$

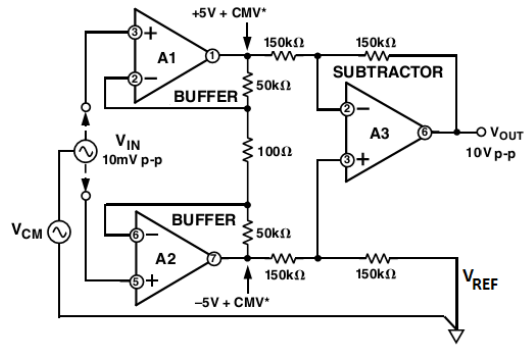


Fig. 2.21. The input buffers of an In-Amp circuit amplify the signal voltage while the common-mode voltage receives unity gain. However, the common-mode voltage is then rejected by the In-Amp’s subtractor section. Redrawn and adapted from [20].

Thus, amplifier A3’s output will be equal to the difference between $V_{OUT_{A1}}$ and $V_{OUT_{A2}}$ as exposed in Equation 2.12.

$$V_{OUT_{A3}} = V_{OUT_{A1}} - V_{OUT_{A2}} = 5V + CMV - (-5V + CMV) = 10V \quad (2.12)$$

Because of the symmetry of this configuration, common-mode errors in the input amplifiers tend to be cancelled out by the output stage subtractor. Ideally, the common-mode voltage will be totally cancelled, but in fact, this factor is impossible to cancel completely, since the manufacture conditions and material temperature are dependent on the In-Amps, which are not ideal.

BITalino - Architecture Description

The main goal of this work was to develop a versatile platform that integrates multiple measurement sensors for bioelectrical and biomechanical data acquisition. BITalino was designed as a set of modular blocks to allow maximum versatility. Targeting the acquisition of physiological signals, the analog front-end integrates individual sensor blocks for Electrocardiography (ECG), Electromyography (EMG), Electrodermal Activity (EDA) and Accelerometry (ACC). Additionally, BITalino also provides a Light sensor (LUX) and a Light-Emitting Diode (LED) blocks, to enable synchronization with third-party equipment (e.g. synchronization with a computer screen or a video camera). The digital back-end is supported by a control block based on a Micro-controller Unit (MCU), a power management block (regulation and battery charger), and a wireless communication block that uses a Class II Bluetooth module (CSR chipset). Figure 3.1

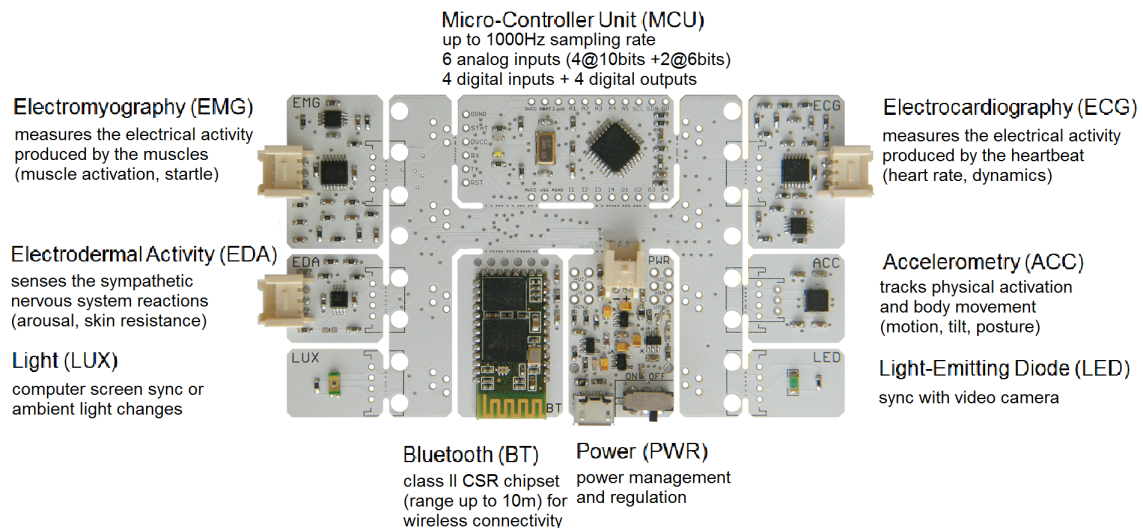


Fig. 3.1. BITalino architecture overview.

illustrates the overall architecture of the platform, while the main specifications of BITalino are summarized in Table 3.1.

Table 3.1. BITalino specifications.

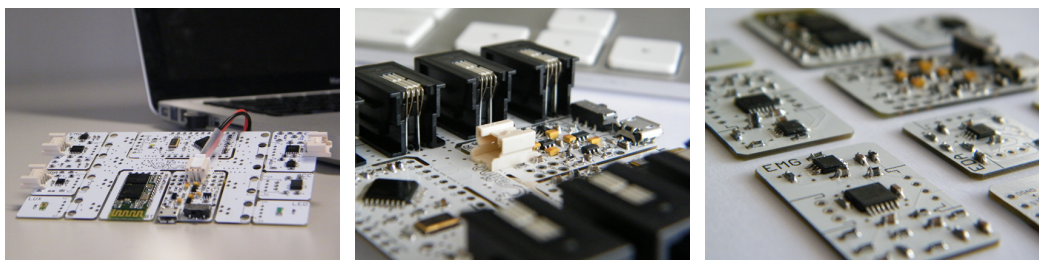
	Specification
MCU	ATMEGA328P - AVR 8-bit RISC
Clock	$8MHz$
Power	$V_{cc} = 3.3V$; $V_{ss} = 1.65V$; $GND = 0V$
Battery	Polymer Lithium Ion - $3.7V - 500m\text{Ah}$
Data Link	Class II Bluetooth v2.0 (range up to 10 m) - 115200 bps [Baud]
Sensors	ECG; EMG; EDA; ACC; LUX
Actuators	LED
Weight	$30g$
Size	$105 \times 60 mm$

All of the BITalino biosignal sensors were designed according to what is defined in the reference literature and taking into account the technical requirements commonly used in terms of bandwidth, dynamic range and physiological principles.

A custom firmware was designed and developed to command the behaviour of the BITalino, enabling the configuration of multiple acquisition parameters. During the acquisition, the signals are sampled and the digitalized data is sent in real time via Bluetooth to the base station (e.g. computer, smart phone, tablet, embedded system). Bluetooth technology was adopted to ensure that there is electrical isolation of the BITalino user from high voltage power sources and because it is also one of the wireless standard interfaces available in multiple devices. Moreover, targeting the low power consumption, all the Integrated Circuits (ICs) in the system are proper for low power applications and only a single Battery cell of Polymer Lithium Ion ($3.7V$) is needed to feed the system.

By default, the system comes as a single board, with its on-board sensors pre-connected to the control block. Nevertheless, all blocks (control, power, communication and sensors) were designed as general purpose, enabling each individual block to be detached from the main board, allowing users to use it in three different configurations:

- **Board:** the board is used without modifications, with its on-board sensors all connected (Figure 3.2a). This configuration allows the users to simply experiment with the on-board sensors;
- **Plugged:** all sensors are detached from the main board (adding RJ22 plugs), leaving only the control, power and communication blocks (Figure 3.2b). This configuration allows the users to implement customized sensor configurations, or even to add their own sensors connected with cables;
- **Freestyle:** all the blocks (control, power, communication and sensors) are detached from the main board (Figure 3.2c), allowing the users to combine them in many different ways that best suit their own projects.



(a) Board. (b) Plugged. (c) Freestyle.

Fig. 3.2. All BITalino versions.

3.1 Analog front-end

In this section we describe each of the sensors (ECG, EMG, EDA, ACC, LUX) and the actuator (LED) that the BITalino platform integrates. All the sensors are single-ended ($0 - 3.3\text{ V}$) and the sensors that measure biosignals (ECG, EMG and EDA) also need an auxiliary mid-supply voltage ($V_{ss} = 1.65\text{ V}$) as a virtual ground.

As described in Chapter 2, there are different types of measurement principles that can be used, namely: voltage potential differential principles (ECG and EMG)[61]; Conductance/Resistance, such as those based on the basic principles of electrical current (EDA)[62]; and Biomechanics which are based in acceleration and MEMS technology (Accelerometry)[63]. Table 3.2 summarizes the physiological parameters used as requirements for the sensors that BITalino integrates,

in terms of dynamical range, and frequency content. The sensors specifications are detailed in the following subsections.

Table 3.2. A summary of the physiological signals parameters.

Modality	Range	Frequency
ECG	$0.5 - 4mV$	$0.01 - 250 Hz$
EMG	$0.1 - 5 mV$	$10 - 450 Hz$
EDA	$1 - 500 k\Omega$	$0.01 - 1 Hz$
ACC	$\pm 1.5 G$	$0 - 10 Hz$

3.1.1 ECG and EMG

The ECG and EMG sensors are based on the voltage potential differential principle. As described in Section 2.1 and 2.2, typically, those signals have amplitudes on the order of a few millivolts ($< 5mV$). The voltage of such signals must be amplified to levels suitable for recording. Thus, it should be amplified (1000 or greater), without attenuation, and with all frequencies present in the desire signal. Accordingly, to measure the low potential differences associated with these signals, both include a precision Instrumentation Amplifier (In-Amp) INA333 [21], offering high common-mode rejection ($110dB$ at $G \geq 10$). They also have low-noise high speed Operational Amplifiers (Op-Amp) AD869x [64] to perform bandpass filtering and amplification.

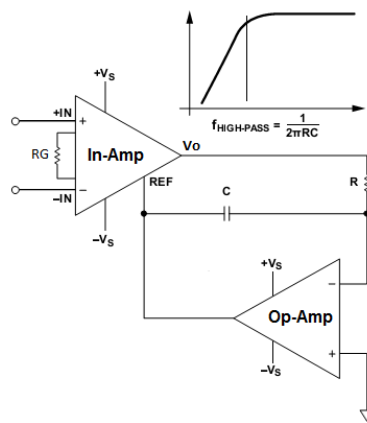


Fig. 3.3. The In-Amp with AC coupling for DC suppression. Redrawn and adapted from the datasheet of AD8221.

The realization of the first stage of the physical amplifier in both circuits (ECG and EMG) is derived from the classical configuration of the In-Amp with three amplifiers, as described in Section 2.7, with an additional stage of AC-coupling. This approach is specially attractive because it allows a precise control of DC levels (rejecting undesired DC offset voltage introduced by electrode-skin interface, as seen in Section 2.5) and, simplifies the design of fast-recovery circuits, which quickly reset the proper DC level after input overload. This technique rejects DC input voltages by negative feedback of the amplified output voltage.

As illustrated in Figure 3.3, the DC component is subtracted by feeding the output signal back to the input *REF* of In-Amp, via the integrating network, which results in a first-order highpass response. Equation 3.1 describes the transfer function of this implementation, where s is the Laplace variable $s = \sigma + j\omega$.

$$H(s) = \frac{G}{(1 + \frac{1}{s\tau})} \quad (3.1)$$

The cut-off frequency of the highpass filter obtained in this way depends on the time constant ($\tau = RC$) of the integrator. Thus, the noise impact at low frequencies is also minimized as well as the baseline wander introduced by user breathing activity and motion artefacts.

Moreover, it is also important to provide a lowpass filter to select the frequencies present in the electrophysiological signal of interest. An active topology was chosen to get a better performance and less complexity than a passive one for those given applications.

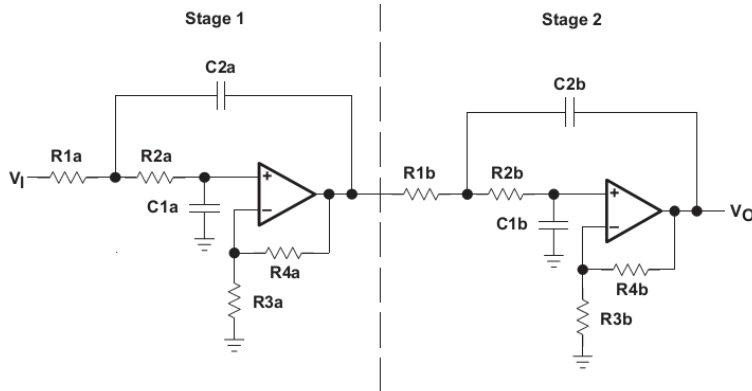


Fig. 3.4. A Sallen-Key circuit implementation - 4th order low-pass filter cascading 2 stages of 2nd order.

A 4th order lowpass Butterworth filter was the circuit implemented, cascading two stages of second-order filter used in Sallen-Key architecture, as illustrated in Figure 3.4. Equation 3.2 describes the transfer function of this implementation, where $\omega = 2\pi f$.

$$H(j\omega) = \frac{\frac{R3_a + R4_a}{R3_a}}{(j\omega)^2 R1_a R2_a C1_a C2_a + j\omega(R1_a C1_a + R2_a C1_a + R1_a C2_a(\frac{-R4_a}{R3_a})) + 1} + \frac{\frac{R3_b + R4_b}{R3_b}}{(j\omega)^2 R1_b R2_b C1_b C2_b + j\omega(R1_b C1_b + R2_b C1_b + R1_b C2_b(\frac{-R4_b}{R3_b})) + 1} \quad (3.2)$$

The block diagram of the ECG sensor circuit can be visualized in Figure 3.5.

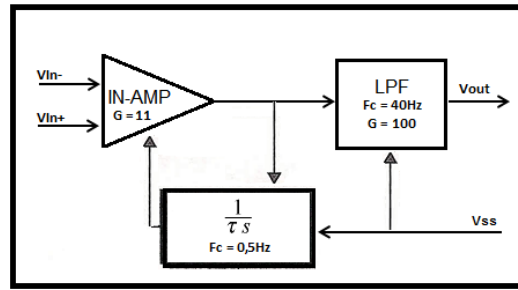


Fig. 3.5. Diagram of the ECG sensor block (*Gain* = 1100; *Bandwidth* = 0.5 – 40 Hz) - An In-Amp with AC coupling to reject DC input voltages followed by a 4th order lowpass Butterworth filter.

The proposed ECG circuit is shown in Figure 3.6. Its frequency response is related with the bandpass filter, as illustrated in Figure 3.7.

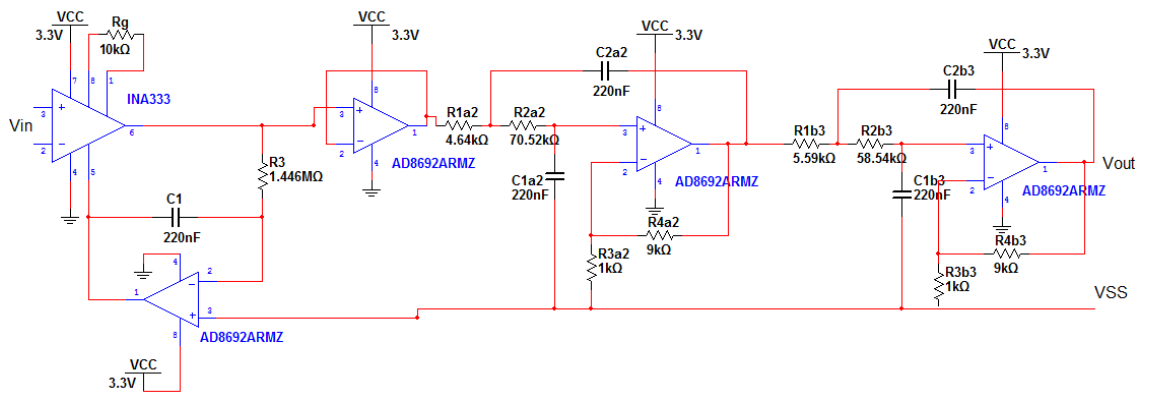


Fig. 3.6. The schematic of the ECG circuit.

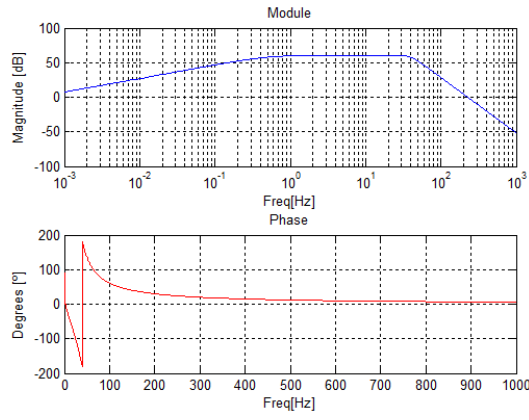


Fig. 3.7. ECG sensor - Frequency response (Gain = 60.83dB and Bandwidth = $0.5 - 40\text{Hz}$).

At each cut-off frequency, there is an attenuation of -3dB . The 1^{st} order highpass filter results in an attenuation of -20dB/decade under the 0.5Hz . The 4^{th} order lowpass Butterworth filter provides -80dB/decade attenuation above the 40Hz , and it has anti-aliasing function.

Equation 3.3 describes the transfer function for this sensor.

$$V_{out} = (V_{IN+} - V_{IN-}) \times 1100 + V_{ss} \quad (3.3)$$

The ECG sensor proposed is specially designed for 1-lead measurement, by placing the electrodes on fingers or hands and then, the lead I can be recorded, as illustrated in Figure 3.8. This approach results in a narrow ECG bandwidth (up to 40Hz) that our circuit design can measure, since it is important to have a rise filtering to reject the signal from high frequency sources, namely, the signal from power lines and its harmonics. However, it is possible to place the electrodes in standard location (e.g. chest) and the leads II, III, V1, V2, V3, V4, V5 and V6 can also be recorded.

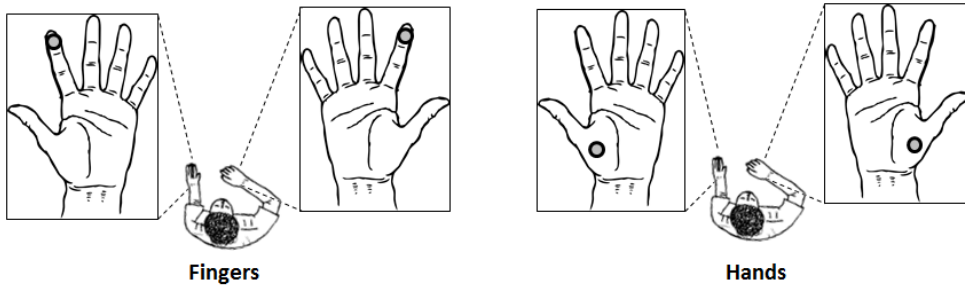


Fig. 3.8. Electrodes placement for ECG acquisition.

The EMG sensor is used for measuring the bioelectrical activity from the muscles, and may be applied to any surface muscle found in standard locations as described in Section 2.2. A block diagram of the EMG sensor circuit can be visualized in Figure 3.9.

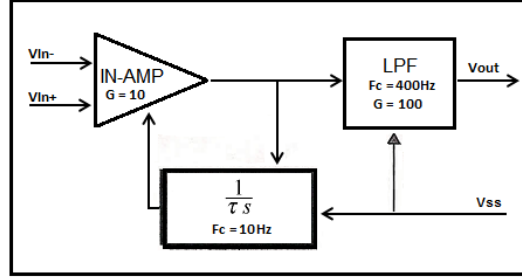


Fig. 3.9. Diagram of the EMG sensor block ($Gain = 1000$; $Bandwidth = 10 - 400\text{ Hz}$) - An In-Amp with AC coupling to reject DC input voltages followed by a 4^{th} order lowpass Butterworth filter.

Similarly to the ECG sensor, it also works using the voltage potential differential principle, and has a bandpass filter but with a wider bandwidth to include, as much as possible, the frequencies present in the electromyographic signal.

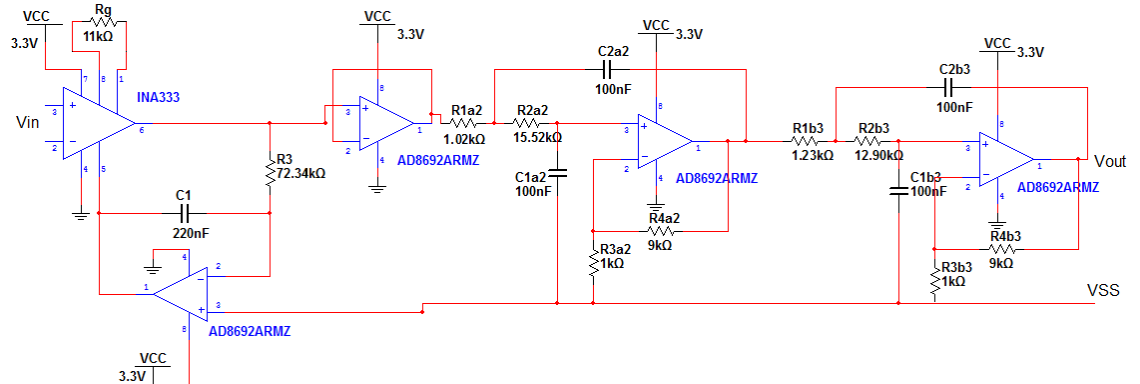


Fig. 3.10. The schematic of the EMG circuit.

The proposed EMG circuit is shown in Figure 3.10 and its frequency response has the same behaviour as the ECG circuit (bandpass filter), however, with the cut-off frequencies at 10 Hz and 400 Hz , as illustrated in Figure 3.11.

Equation 3.4 describes the transfer function for this sensor.

$$V_{out} = (V_{IN+} - V_{IN-}) \times 1000 + V_{ss} \quad (3.4)$$

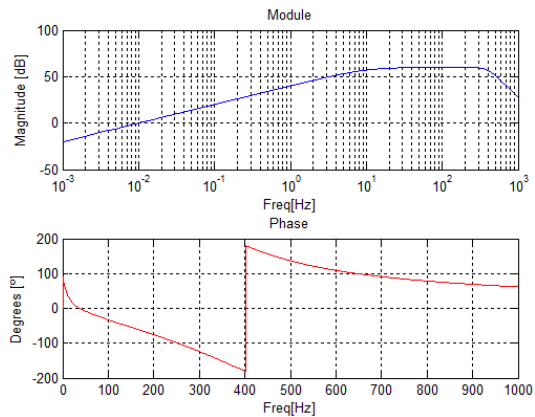


Fig. 3.11. EMG sensor - Frequency response(Gain = 60dB and Bandwidth = 10 – 400 Hz).

The biopotential amplifier circuits (ECG and EMG) described above, with the specific design considerations for each biopotential, allow signal acquisition with acceptable quality in most of the application setups. However, if it is necessary to improve the quality of the signals, in some cases, different approaches can be exploited [65]. These approaches can include an additional third common electrode lead called "driven right leg electrode", "reference electrode" or even "ground electrode", as illustrated in Figure 3.12. This technique is almost universally used since it increases the CMRR of the biopotential amplifier [65]. Both sensors (ECG and EMG) provide a terminal (REF) connected to the V_{ss} which is used as the reference electrode.

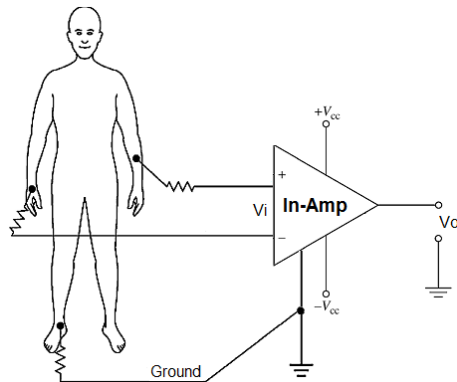


Fig. 3.12. Reference electrode placement in biosignals acquisition. Redrawn and adapted from [19].

In addition, shielding leads and skin preparation enhances signal quality, reduces artefacts and minimizes the need for post-recording artefact rejection. Conductive gel is also recommended

for optimal electrode-skin contact. However, these sensors were designed to be used with dry electrodes and no skin preparation and thus, provide an easy apparatus for biosignals acquisition.

Figure 3.13 illustrates the pinout information that can be useful in case of interfacing with other modules.

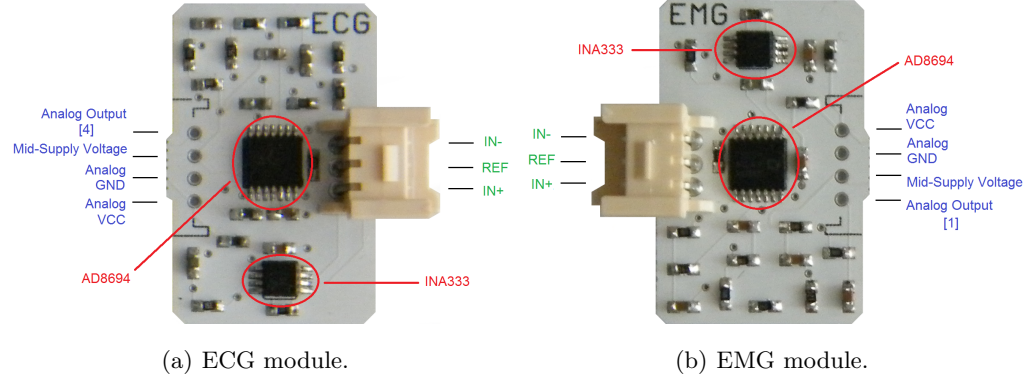


Fig. 3.13. Pinout of the ECG and EMG sensors.

3.1.2 Electrodermal Activity

The EDA sensor was designed to measure the skin conductance, namely, the Skin Conductance Level (SCL) and Skin Conductance Response (SCR). In each case the electrodes are applied at the hand palms or fingers, allowing the measurement of the variations in the skin resistance originated by sweat duct secretion activity. This sensor is based on the Transconductance Amplifier (OTA) circuit, and so it works by injecting a DC current through the skin surface (conductance/resistance) and then measures the voltage associated with it.

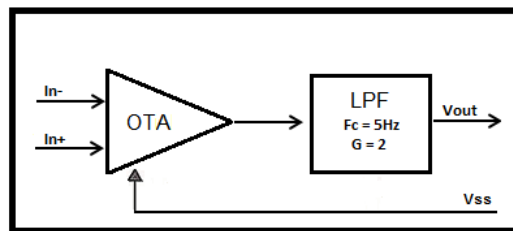


Fig. 3.14. Diagram of the EDA sensor block ($Gain = 2$; $Bandwidth = 0 - 5\text{ Hz}$) - An OTA circuit followed by a 2^{nd} order lowpass Butterworth filter.

The block diagram of this circuit can be visualized in Figure 3.14. The first circuit block provides a constant DC current to inject through the skin surface. This will generate a potential voltage associated with the Galvanic Skin Response. The last stage consists of a 2nd order lowpass Butterworth filter (Gain = 2; fc = 5 Hz) to reject the frequencies that are out of the desired bandwidth, and it has an anti-aliasing function because of the digitalization that occurs afterwards.

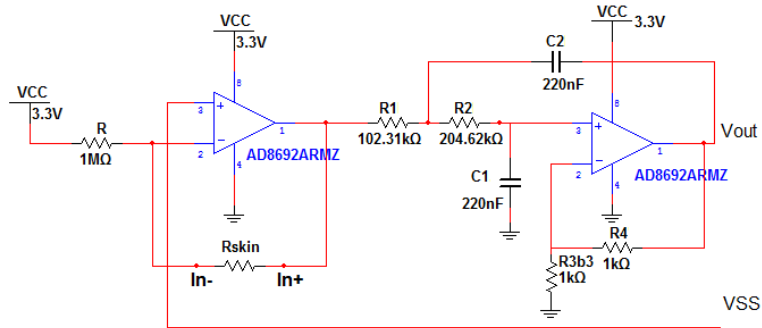


Fig. 3.15. The schematic of the EDA circuit.

The proposed EDA circuit is shown in Figure 3.15 and its frequency response is illustrated in Figure 3.16. At cut-off frequency (5 Hz), there is an attenuation of $-3dB$ and provides a $-40dB/decade$ attenuation above this frequency.

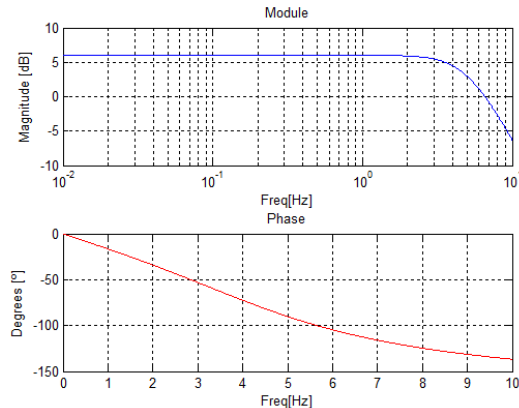


Fig. 3.16. EDA sensor - Frequency response(Gain = 6.02dB and Bandwidth = 0 – 5 Hz).

Equation 3.5 describes the transfer function of the EDA circuit.

$$V_{out} = \left(-\frac{R_{skin}}{R} \times V_{cc} + \frac{R + R_{skin}}{R} \times V_{ss} \right) \times G \quad (3.5)$$

According to [50], the skin resistance often variates between $1k\Omega \leq R_{skin} \leq 500k\Omega$ when injecting a controlled DC current (few μA). However, we decided to assume $R = 1M\Omega$ in our design, ensuring a wide range of measurable skin resistances:

- $R_{skin} = 1k\Omega \rightarrow V_{out} \simeq V_{cc}$;
- $R_{skin} = 1M\Omega \rightarrow V_{out} \simeq 0$.

The value of the resistance R defines the value of the current injected in the user skin. In this case it is assumed that $V_{cc} = 3.3 V$, $V_{ss} = 1.65 V$ and $G = 2$, then:

$$I_{skin} = \frac{V_{cc} - V_{ss}}{R} \Leftrightarrow I_{skin} = \frac{1.65 V}{1M\Omega} = 1.65 \mu A \quad (3.6)$$

Considering a sampling resolution of 10 bits, then:

$$\Delta_V = \frac{3.3 V}{2^{10} - 1} = 3.2 mV \quad (3.7)$$

So, the conductance and the resistance resolution of the circuit are:

$$\Delta_G = G \times \frac{I_{skin}}{\Delta_V} = 2 \times \frac{1.65 \mu A}{3.2 mV} = 1.03 m\Omega^{-1} \rightarrow \Delta_R = 970 \Omega \quad (3.8)$$

As highlighted in Equation 3.8, the resolution of the circuit is delimited by the value of the current injected to the skin surface as well as the number of bits of the Analog-to-digital converter. Figure 3.17 illustrates the pinout information that can be useful in case of interfacing with other modules.

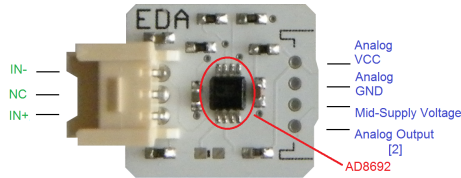


Fig. 3.17. EDA block pinout

3.1.3 Accelerometry, Light sensing and LED actuator

In order to obtain a more versatile platform, an Accelerometer (ACC), a Light sensor (LUX) and a Light-Emitting Diode (LED) were included, as illustrated in Figure 3.18.

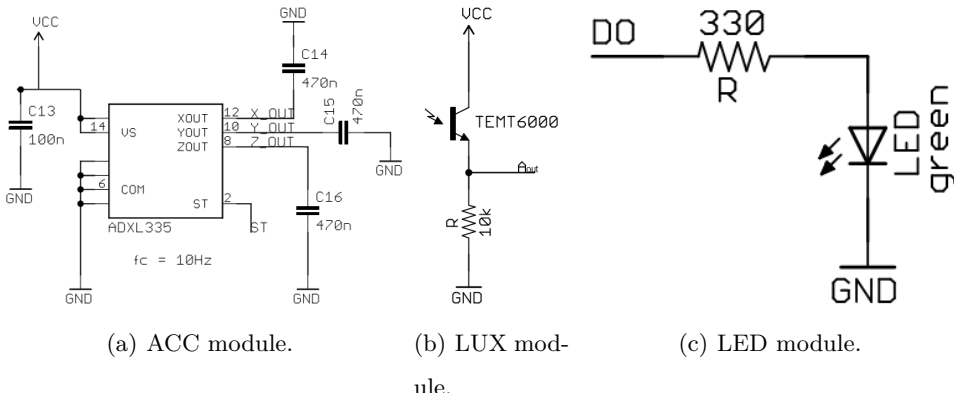


Fig. 3.18. Schematics of the ACC, LUX and LED modules.

To perform a complete 3-axis acceleration measurement system, a small, low power and MEMS based Accelerometer module (ADXL335 designed by Analog Devices [66]) was integrated. This sensor can measure the static acceleration of gravity in tilt-sensing applications, as well as dynamic accelerations, as a vector quantity. This resulting vector can then be used to sense position, vibration, shock, motion, etc, within the dynamic range of the sensor. The product measures acceleration with minimum full-scale range of $\pm 3 G$ with easy bandwidth selection (including external capacitors) to suit the application and it also provides analog output. In our design the bandwidth was selected between $0.5 - 10 Hz$ for all axis (X,Y,Z), as illustrated in Figure 3.18a.

The LUX sensor was included and can be used for optical synchronization with external sources or for ambient light sensing. It can even be used in conjunction with a light source (two wavelengths) to monitor pulse oximetry saturation. This sensor is a type of photodetector capable of converting light into voltage. As illustrated in the Figure 3.18b, this sensor acts as an NPN transistor (Phototransistor - TEMT6000 [67]) and works according to its principles, namely, the more the sensor is exposed to light, the stronger is the base bias and thus, the highest is the output voltage signal. The device is sensitive to the visible spectrum with the wavelengths between $360 - 970 nm$.

The LED module consists of a single Light-Emitting Diode. As illustrated in Figure 3.18c, it is directly connected with a digital output of the MCU and can be used to send synchronization signals to external devices, to trigger external interfaces or even as a visual feedback indicator when associated with a signal threshold.

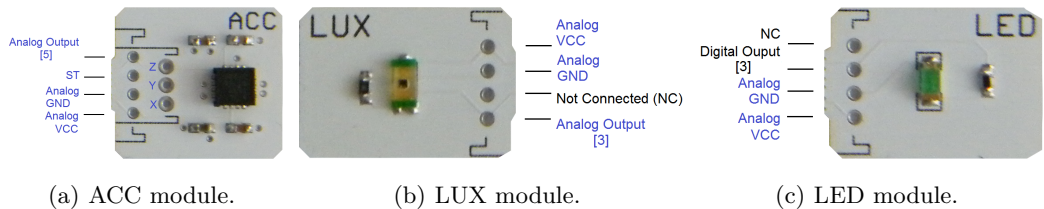


Fig. 3.19. Pinout of the ACC, LUX and LED modules.

Figure 3.19 illustrates the pinout information that can be useful in case of interfacing with other modules.

3.2 Control, Power and Communication

The Control, Power and Communication modules represent the "Core" of the BITalino board. The main purpose of the Control block is to provide a physical support to the system behaviour. With proper firmware, the Micro-controller Unit (ATmega328P) provides access to the peripherals. Sourced by a very precise $8MHz$ external Quartz Crystal with $\pm 20ppm$ of frequency stability and tolerance, together with an optimized firmware, it ensures an high accuracy conversion of the analog signals from the sensors to a digital format. The ATmega328P is a low-power CMOS 8-bit Micro-controller based on the AVR enhanced RISC (Reduced Instruction Set Computer) architecture, which executes powerful instructions in a single clock cycle with throughputs approaching of 1MIPS per MHz [22]. Figure 3.20 represents the block diagram of the MCU core, where are highlighted, in red, the peripherals and cores used, and Figure 3.21 illustrates the pinout information that can be useful in case of interfacing with other modules.

The Power management block provides voltage regulation to all the BITalino modules and it is also fitted with a charger controller that manages the battery charging process.

Sensitive analog components such as the amplifiers and the analog-to-digital converters are often contaminated by a small amount of digital noise. Although all the BITalino modules work with nominal voltage of $3.3V$, it is always a good circuit design principle to separate analog (AVCC) and digital (DVCC) voltage regulation and ground planes (AGND and DGND) as well. This technique provides higher isolation between them, as illustrated in Figure 3.22.

Accordingly, the Communication block (which integrates the Bluetooth module) is the module which may inject amount of noise through the power supply lines onto the analog blocks. Therefore, it was decided to separate its power supply (DVCC and DGND). A low-dropout (LDO) linear voltage regulator (TPS73001 [24], Figure 3.23b)) suitable for Wireless applications

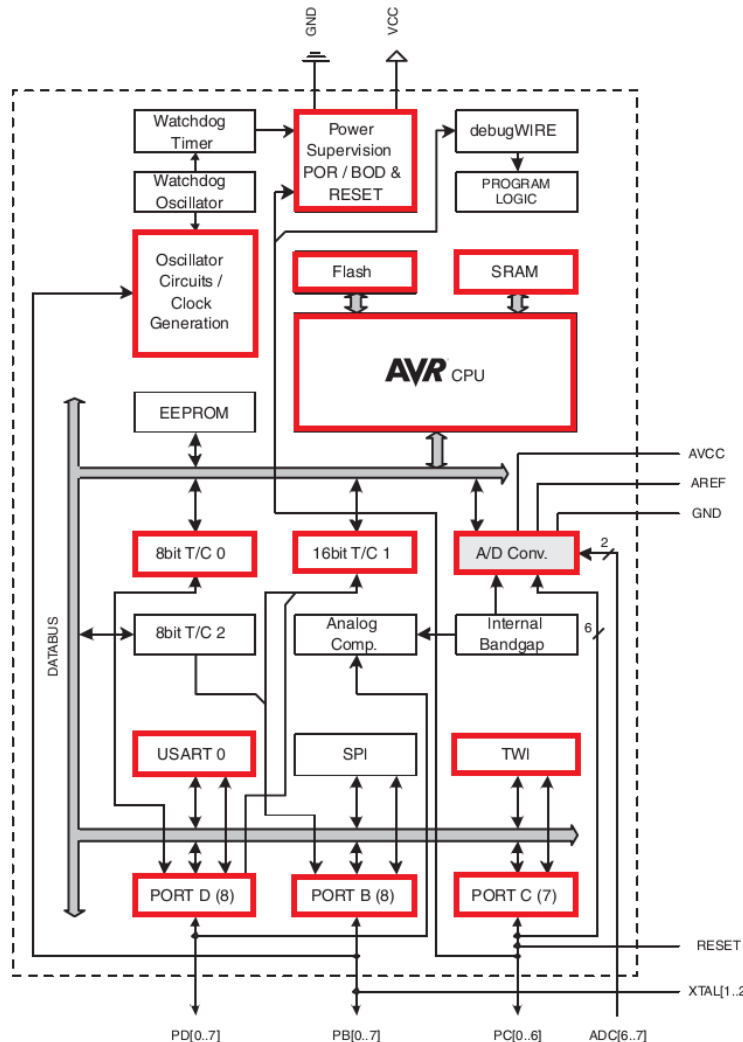


Fig. 3.20. Hierarchical diagram of the MCU module. Redrawn and adapted from [22].

was integrated to provide a voltage regulation (DVCC). On the other hand, the other modules (MCU and sensors) are then supplied by another voltage regulation (AVCC). The AVCC is provided by an efficient linear voltage regulator (MIC5205 [23], Figure 3.23a)) with high output voltage accuracy (better than 1%) proper for battery powered devices.

As already focused in Section 3.1, each sensor is single-ended and operates with single supply voltage between 0 V to 3.3 V . Therefore, one of the system requirements was to furnish a mid-supply reference voltage (a virtual ground of $V_{ss} = 1.65\text{ V}$). A stable reference voltage was

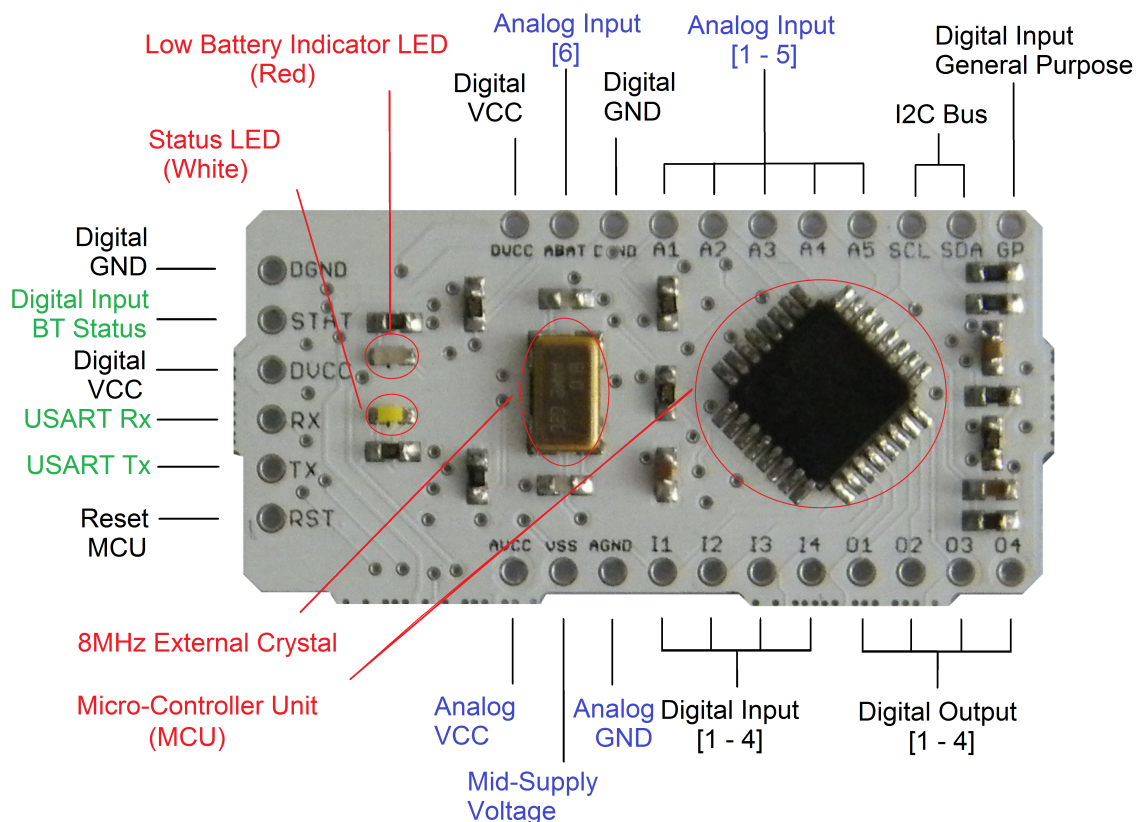


Fig. 3.21. Control block pinout.

provided using a voltage divider directly connected to a voltage follower (Buffer), as illustrated in Figure 3.23c.

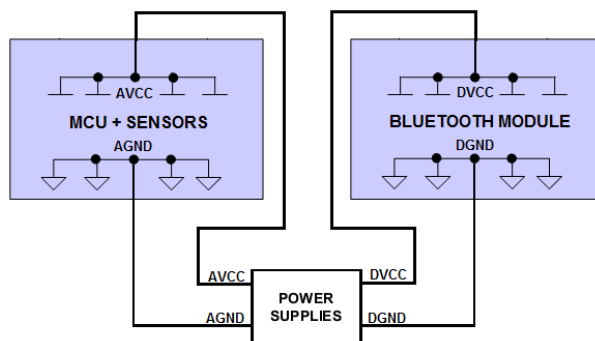


Fig. 3.22. Power Supply Isolation between Analog and Digital circuits.

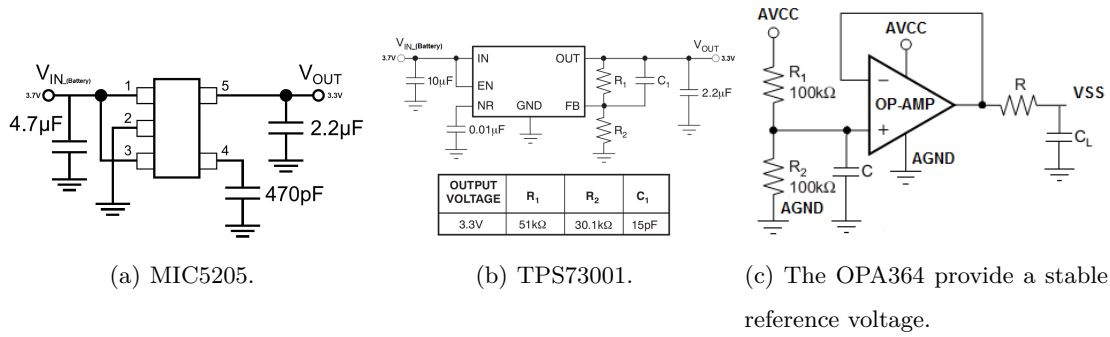
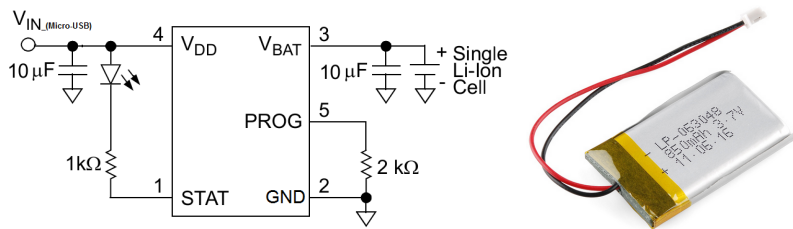


Fig. 3.23. Voltage regulators included in the Power block. Redrawn and adapted from [23, 24, 25], respectively.

The battery charger management is ensured by an highly advanced linear charge management controller (MCP73831 [26]) which employs a Constant-Current/Constant-Voltage charge algorithm. It works through continuous monitoring of the Battery voltage and if the voltage drops below the recharge supply source (from Micro USB - typically 4.2 V), a charge cycle begins. At first, the current is supplied to the Battery (Constant-Current mode). When the limit of the charge current, based on the temperature, exceeds 150°C , the charge changes to Constant-Voltage mode. The charge cycle is finished when, during Constant-Voltage mode, the average charge current diminishes below a percentage of the programmed charge current (max. 0.3%) based on the value of the resistor connected to the PROG pin ($2\text{k}\Omega$ - 500m A), as illustrated in Figure 3.24a) [26].



(a) Battery Charger Management circuit. (b) Example of a Polymer Lithium Ion Battery.

Fig. 3.24. Power management circuit and battery. Redrawn and adapted from [26, 27], respectively.

Charging is made when the device is turned off and connecting a power supply source via Micro-USB. A Polymeric Positive Temperature Coefficient device (PPTC, commonly entitled as a Resettable fuse) was also included between the recharge supply source (Micro USB) and the

battery charger management, as an interface which protects against over-current faults (tripping current - 1 A).

The Power block is prepared to be preferentially sourced by a Polymer Lithium Ion Batteries (nominal 3.7 V at 500m Ah - minimum)). Figure 3.24b) shows an example of a Polymer Lithium Ion Battery which can be used with the BITalino. Figure 3.25 illustrates the pinout information that can be useful in case of interfacing with other modules.

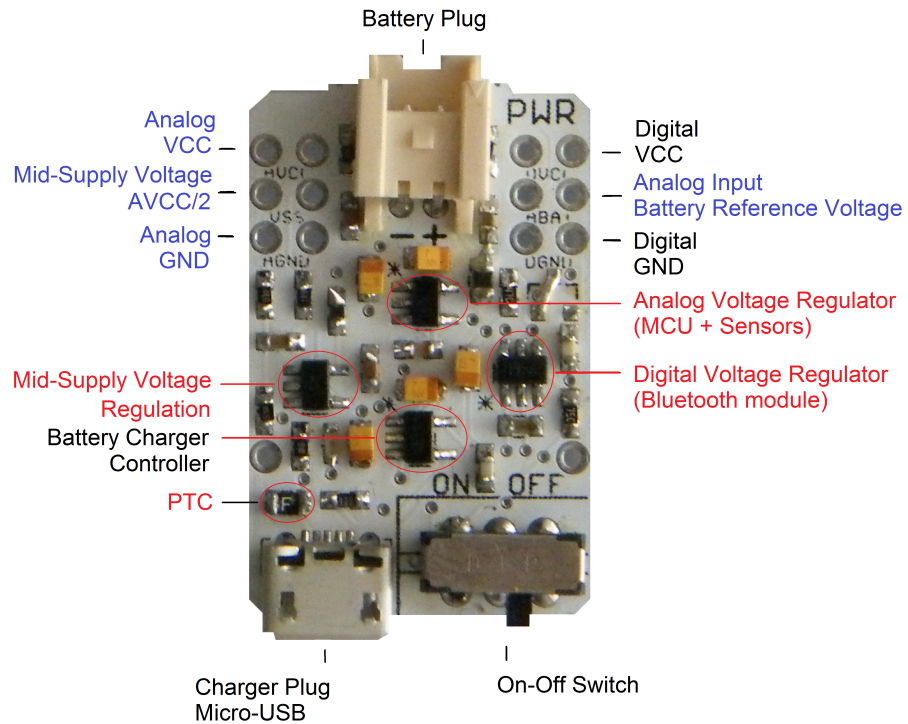


Fig. 3.25. Power block pinout.

Our goal was to develop a versatile wireless platform with multiple sensors. Nowadays, Bluetooth has become an increasingly used wireless technology standard for exchanging data over short distances. It was designed for low power consumption, and this technology allows easy connection (pairing) and communication between Bluetooth devices with security, being available in multiple devices, such as mobile phones, consumer electronics, PCs, automotive, health and wellness, sports and fitness and smart home industries [68]. Although the Bluetooth technology was adopted to ensure real-time data streaming between the BITalino and a third-party device (e.g. computer, mobile phone, tablet, embedded system), it is also important since it provides

a galvanic isolation to the BITalino user. Configured to work as a slave Bluetooth device, the BITalino Bluetooth module is loaded with SPP (Service Pack for Proliant) firmware for UART wireless cable replacement functions with throughputs up to $3MHz$ EDR (Enhanced Data Rate).

The Bluetooth module (EGBT-045MS) is a Class II Bluetooth v2.0 module and it is directly connected to the MCU block via USART bus with a baudrate of $115200\ bps$. Figure 3.26 illustrates the pinout information that can be useful in case of interfacing with other modules.

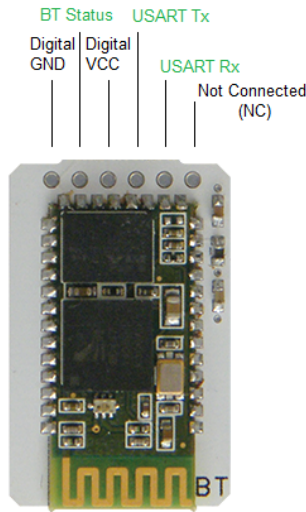


Fig. 3.26. Bluetooth block pinout.

3.3 Firmware

As previously mentioned, the firmware defines the overall behaviour of the system, and controls the data streaming over Bluetooth. The system allows the acquisition of 6 analog input ports (4 with 10 bit + 2 with 6 bit) and also exposes 8 digital ports (4 input + 4 output).

The system has three operation modes, and has a set of commands that can be used to configure the device. The global operation workflow is represented in Figure 3.27.

The configurable settings on the system are changed by sending 1 byte commands from the base station to the device; Figure 3.28 summarizes the modes and commands which are interpreted by the system.

The available operational modes are:

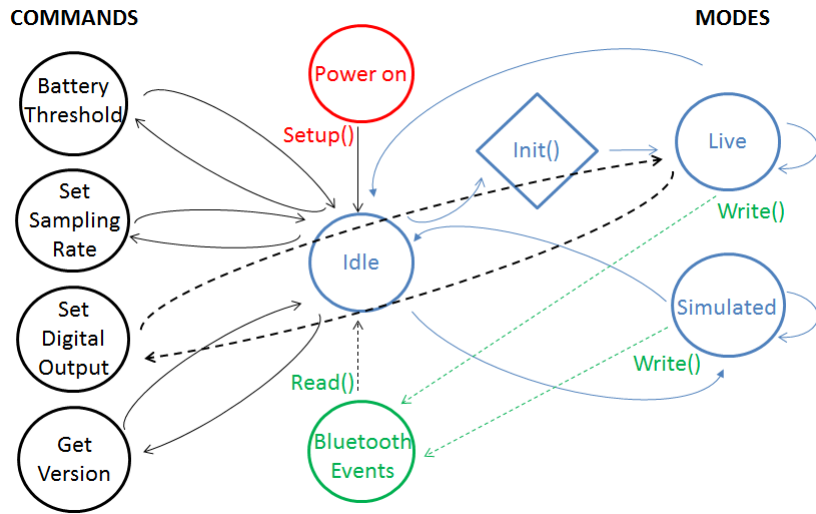


Fig. 3.27. State diagram of the firmware operation.

- 0) *Idle*: The system disables any mode in which it is in, and remains on standby until it receives a command from the base station to change the mode or to adjust the settings. The status LED blinks in fading style controlled by the PWM (Pulse Width Modulation) output.
- 1) *Live*: In this mode, the status LED changes and it blinks with a frequency of 2 Hz. The system continuously samples all input analog and digital channels, packs the data into a set of bytes, and sends the data packets through the USART controller. In order to make the most efficient use of the available bandwidth on the communication channel, the packet is optimized and its size depends on the number of channels acquired in each period. The packet has a maximum size of 8 bytes and a minimum size of 3 bytes; it includes also a sequence number and a 4-bit Cyclic Redundancy Check (CRC) value, based on Linear Feedback Shift Register (LSFR) function with the polynomial generator ($g(X)$) described in Equation 3.9

Modes:	
0 0 0 0 0 0 0 0	→ Idle mode
A5 A4 A3 A2 A1 A0 0 1	→ Live mode with analog channel selection
A5 A4 A3 A2 A1 A0 1 0	→ Simulated mode with analog channel selection
Commands:	
Threshold 0 0	→ Battery threshold definition (when in <i>idle mode</i>)
- - D03 D02 D01 D00 1 1	→ Set digital output (when in <i>live mode</i>)
Fs - - - - 1 1	→ Sampling Rate definition (when in <i>idle mode</i>)
- - 0 0 0 1 1 1	→ Get firmware version (when in <i>idle mode</i>)

Fig. 3.28. Modes and commands of the system operation.

and implemented by the state diagram illustrated in Figure 3.29, to detect possible errors in the message.

$$g(X) = X^4 + X + 1 \quad (3.9)$$

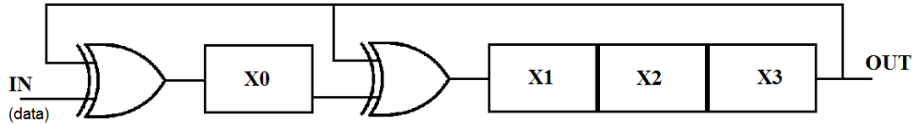


Fig. 3.29. A 4-bit LFSR with its state diagram. The XOR gates provide feedback to the registers that shift bits from left to right.

The packing process is done using bitwise operators, and the packet structure can be seen in Figure 3.30.

		Bits							
		7	6	5	4	3	2	1	0
Bytes	7	S	S	S	S	CRC	CRC	CRC	CRC
	6	D0	D1	D2	D3	A0	A0	A0	A0
	5	A0	A0	A0	A0	A0	A0	A1	A1
	4	A1	A1	A1	A1	A1	A1	A1	A1
	3	A2	A2	A2	A2	A2	A2	A2	A2
	2	A2	A2	A3	A3	A3	A3	A3	A3
	1	A3	A3	A3	A3	A4	A4	A4	A4
	0	A4	A4	A5	A5	A5	A5	A5	A5

Fig. 3.30. Data packet structure.

The BITalino Bluetooth has a pin flag which sets (high voltage level - 3.3 V) while a base station is paired with it. One additional digital input of the MCU is continuously reading the level of this flag pin; when its level is low (0 V), as such if the connection was closed or lost abruptly, the machine state goes to the Idle mode again and waits for another Bluetooth connection;

- 2) *Simulated:* Although it is similar to what is done in the *Live* mode. In this mode the system will simulate the acquisition process by transmitting synthesized signals. These correspond to sinusoidal (A2-A4) and square waves (D0-D3), white noise (with Normal Distribution) (A1) as well as a synthetic ECG wave (A0), as illustrated in Figure 3.31. The data packet structure

is the same as before. This way, the communication and interaction between the base station and the BITalino can be tested.

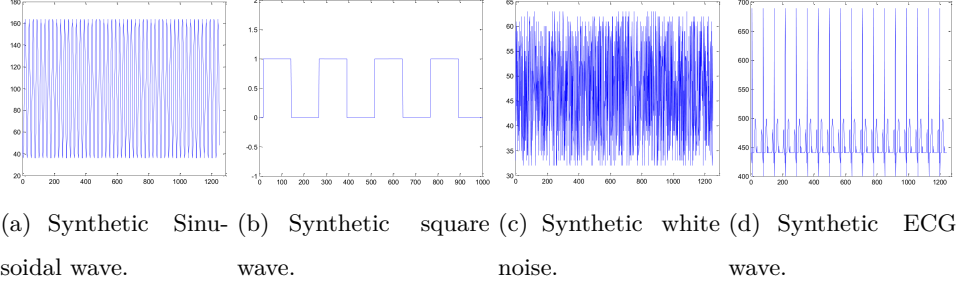


Fig. 3.31. Synthesized waves related to the Simulated mode.

The available operational commands are:

- 0) *Threshold*: This command is used to define the threshold for the low battery LED indication. One of the analog input ports (A5) is continuously acquiring the voltage level of the battery; when its level is lower than the threshold initially defined, the red LED included in the Control block is turned on. By default, the threshold value is $3.4V$, however it can be changed between $3.4 - 3.8V$.
- 1) *Set Digital Output*: With this command, the system activates or deactivates physical digital output ports, according to the information on the channel mask defined.
- 2) *Sampling Rate*: This command is used to define the sampling rate for data acquisition; In Table 3.3 we present the valid values for this command.

Table 3.3. Sampling rate definitions.

Sampling rate (Hz)	1000	100	10	1
10^{F_s}	10^3	10^2	10^1	10^0

- 3) *Get Version*: This command is used to get a message with the information of the firmware version, i.e "BITalinoV3.10 – 20130710\n".

3.3.1 Real-time acquisition

The most important requirement of the system is during the *Live* mode, to ensure an accurate sampling rate. The approach designed was based on timer interrupts, and as such an ISR (In-

terrupt Service Routine) was implemented on Timer 1 and another on Timer 0, as illustrated in Figure 3.32. The ISR on Timer 1 (16 bits) defines the sampling rate and it is programmed to set the analog to digital converter (ADC), sample each channel and fill a circular buffer (FIFO). On the other hand, the ISR on Timer 0 (8 bits) gets the samples from the buffer, packs all the data and calculates the CRC before sending the data packets through the USART controller, and consequently to the Bluetooth module. Both are programmed in Clear Timer on Compare match (CTC) mode and Timer 1 has higher priority when both occur in the same period of time. It is extremely important that the samples inside the buffer are retrieved quicker than the production rate; as such, Timer 0 requires a system call 4 times more frequently than Timer 1 does. Otherwise, there would be an overflow inside the buffer and consequently the data would be corrupted. The read-modify-write operations, to process the data between the two ISRs, are protected by the atomic operation that compose each of them.

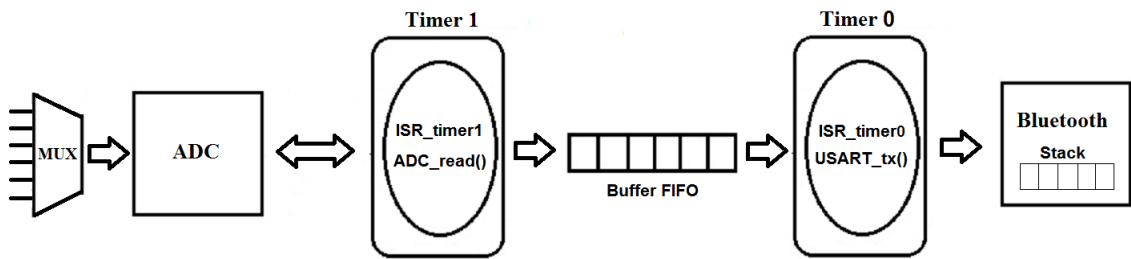


Fig. 3.32. State diagram of the acquisition process.

4

Evaluation Tests

We performed exhaustive tests to all the BITalino versions to evaluate the data integrity and the waveform properties of the signals acquired, the digital and analog blocks performance, and power consumption. This chapter is divided in two parts: 1) qualitative test - visually verify the correct operation of the board; 2) quantitative tests - formal evaluation of the board performance, using the typical measures within the instrumentation field [69].

4.1 Qualitative tests

During the qualitative tests we evaluated the data integrity, the waveform properties of the acquired signals, and the communication process between the BITalino and the base station.

As a result from other research work [70], a biosignal visualization software framework was developed for direct interaction with the BITalino, entitled "SignalBIT". Running in a base station, the SignalBIT is responsible for configure, operate and receive the acquired data from the BITalino. The interaction is provided by the menu window, shown in Figure 4.1, which directly interacts with the BITalino (Start/Stop acquisition), choose acquisition configurations such as, sampling rate and the number of channels to be acquired. Furthermore, when the user starts a new recording session, the signals start to appear in each corresponding plot and thus, allows the signals visualization in real-time. Additionally, it is also possible to save the recorded data for later processing. The front-end is based on Web technologies (HTML5 and CSS3) that displays the user interface and allows all the interaction. The back-end is implemented in Python, which is responsible for the connection with the BITalino via Bluetooth and for all the data processing and storage. The communication between the front-end and the back-end is based on the WebSocket standard, which implements a full-duplex single socket connection.

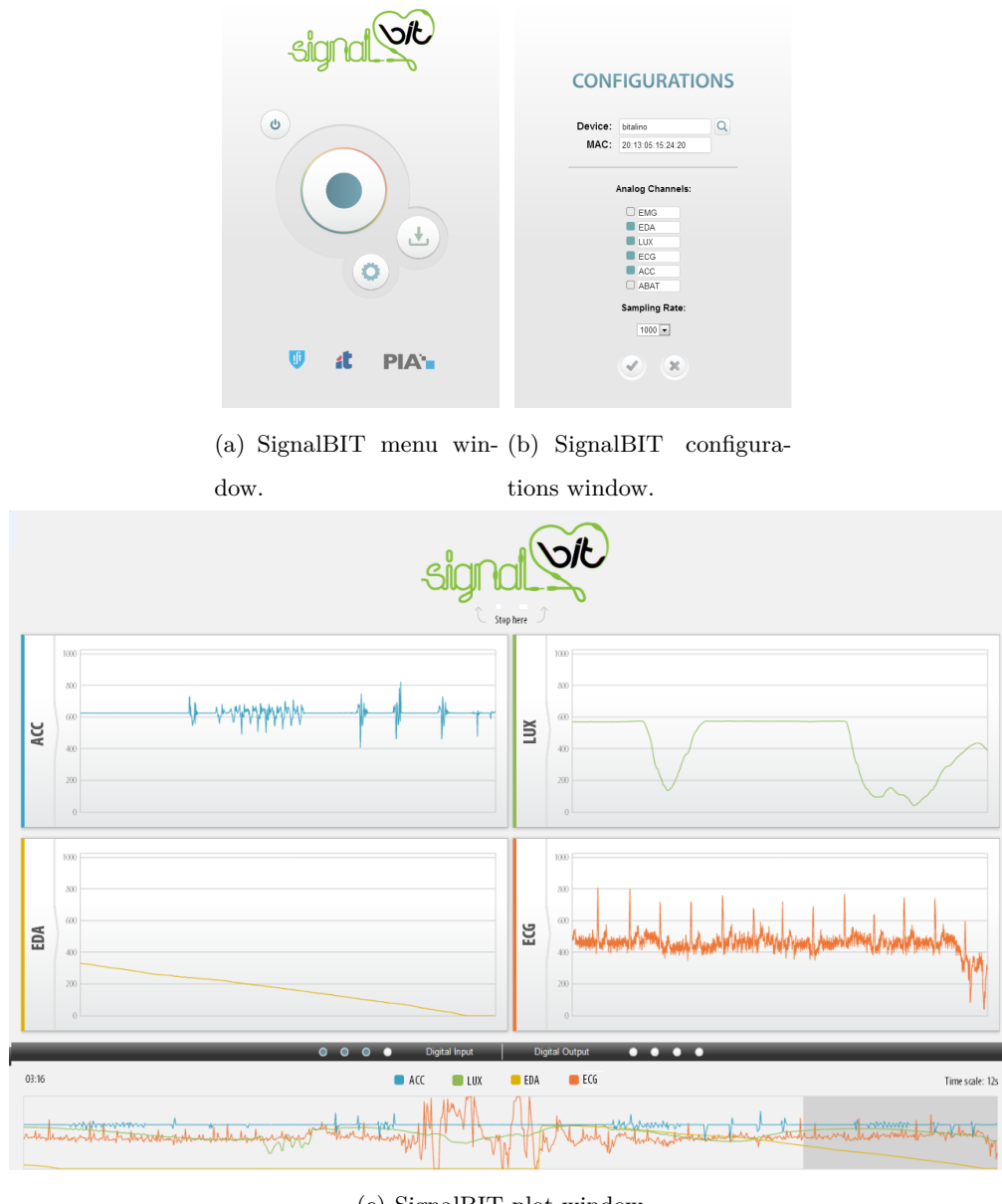


Fig. 4.1. SignalBIT application user interface.

Using the SignalBIT, we evaluated the real time acquisition process (3×17 hours) as well as the communication between the BITalino and the base station. The experimental results have shown that the data collected through the proposed system preserves the waveform properties for all BITalino acquired signals and ensures 100% of data integrity (distance up to 10m in free space).

More comparative tests were also performed between the BITalino ECG sensor and a conventional medical-grade equipment (Philips PageWriter Trim III ECG device), published as a result from other research work [71]. The results have shown that the signals obtained through the BITalino ECG sensor are matched to the conventional lead I derivation, and the morphology of the heartbeat waveform can be retrieved.

4.2 Quantitative tests

Tests were performed to the BITalino, to check both the digital and analog blocks, namely, the temporal uncertainty (such as, sampling rate accuracy); the dynamic specifications of the Analog-to-Digital Conversion (such as, ENOB: Effective Number of Bits); and the quality of the analog front-end (SNR: Signal-to-Noise Ration, SINAD: Signal-to-Noise Ration plus Distortion and THD: Total Harmonic Distortion). In all analog experimental tests, the signals were generated using an Agilent 33220A Function Waveform Generator (with 14-bits resolution, sampling rate of 50MSa/s and Harmonic distortion of $-70dBc$ (DC to $20kHz$)).

To characterize the temporal uncertainty of the three versions of the BITalino, a synthesized ramp wave with a frequency of $1kHz$, with $3V_{pp}$ and offset of $V_{CC}/2$ was acquired and its slope ($\frac{\Delta V}{\Delta t}$) was analysed and compared with what was really injected. Table 4.1 summarizes the sampling rate accuracy results; only the higher sampling rate ($F_s = 1kHz$) was tested as it is the most demanding in terms of sampling accuracy. This test characterizes the accuracy of the clock source as well as the performance of the firmware while in acquisition (Live mode).

Table 4.1. Temporal uncertainty of the three versions of the BITalino (Board, Plugged and Freestyle).

BITalino version	F_s (real value)[Hz]	Skew [%]	Jitter [%]
Board	999.9914 ± 0.025	0.00086	0.0025
Plugged	999.9957 ± 0.025	0.00043	0.0025
Freestyle	999.9871 ± 0.018	0.00129	0.0018

The ATmega328P features a 10-bit Successive-Approximation-Register (SAR) Analog to Digital Converter (ADC) which it runs with an input clock frequency of $200kHz$ ensuring maximum resolution. The ADC is connected to a 6-channel Analog Multiplexer with single-ended voltage inputs ($0 - 3.3V$).

To quantify the quality of the ADC we calculated the ENOB, SNR, SINAD and THD, typically used for determining the ADC dynamic specifications [72].

The signal-to-noise ratio (SNR) measures the ratio of the AC signal power to noise power below one-half of the sampling frequency, as Equation 4.1 describes, where P_s is the signal power, and P_n is the noise power (exclude harmonic signals and DC).

$$SNR(dB) = 10 \log_{10} \frac{P_s}{P_n} \quad (4.1)$$

THD is the sum of the powers of the harmonic components (spurs) rationed to the input signal power, as Equation 4.2 describes, where P_d is the power of all the specified spectral components (harmonics).

$$THD(dBc) = 10 \log_{10} \frac{P_d}{P_s} \quad (4.2)$$

SINAD is the calculated combination of SNR and THD. It is the ratio of the amplitude of the fundamental input signal to the sum of all other spectral components below one-half of the sampling frequency (excluding DC), as Equation 4.3 describes. The theoretical minimum for SINAD value is equal to the ideal SNR (Equation 4.4) with SAR ADCs, where n is the number of bits.

$$SINAD(dBc) = 10 \log_{10} \frac{P_s}{P_n + P_d} \quad (4.3)$$

$$SNR(dB)_{ideal} = 6.02n + 1.76 = 6.02 \times 10 + 1.76 = 61.96[dB] \quad (4.4)$$

The ENOB can be calculated as in Equation 4.5.

$$ENOB = \frac{SINAD - 1.76}{6.02} \quad (4.5)$$

A higher ENOB means that the voltage levels recorded in an analog-to-digital conversion are more accurate.

Table 4.2 shows the results of the ADC dynamic specifications when the sampling rate is 1k Hz. Dynamic tests are typically made applying an analog signal with voltage range of 95% of the full-scale range of the ADC. Then, a synthesized sine wave with a frequency of 15 Hz was used for this purpose.

The crosstalk between each channel was also tested, and it is less than the ideal SNR ($-61.96[dB]$) for 10-bits resolution.

Table 4.2. Dynamic specifications of the ADC (15 Hz sine wave; $F_s = 1k\text{ Hz}$).

SNR [dB]	SINAD [dBc]	THD [dBc]	ENOB [bits]
55.72	54.29	-59.80	8.73

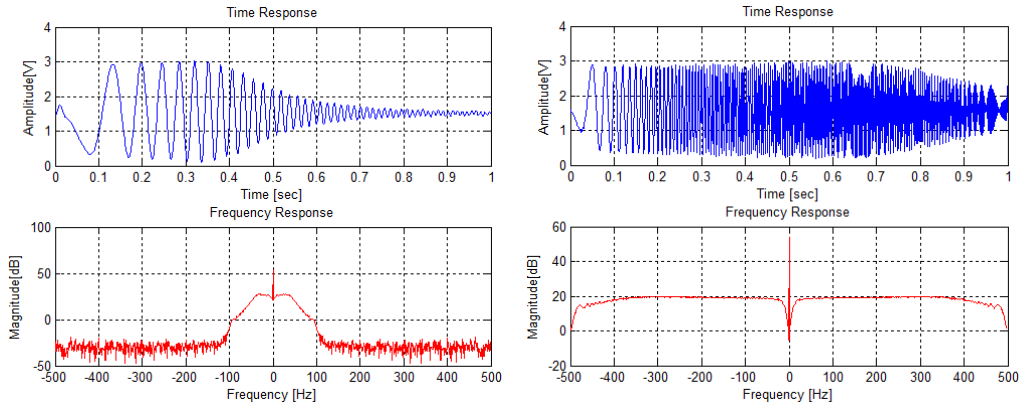
To characterize the dynamic specifications of the analog circuits such as the ECG and EMG blocks, a synthesized sine wave with frequency of 24 Hz and 55 Hz, respectively, with 25mVpp and offset of $V_{CC}/2$ were used, and the gain of each sensor was reduced to 100 (In-Amp with unity Gain). This procedure ensured a desirable output signal without saturation and ranged between 0 – 3.3 V. Table 4.3 summarizes the results of the dynamic specifications of the circuits of the three versions of the BITalino (Board, Plugged and Freestyle). Where significant variations between the three versions were not found.

Table 4.3. Dynamic specifications (ECG and EMG, $F_s = 1k\text{ Hz}$).

	Sensor		SNR[dB]	SINAD[dBc]	THD[dBc]
Board	ECG		37.38	37.11	-49.39
	EMG		35.96	35.86	-52.03
Plugged	ECG	short*	39.39	36.58	-39.80
		long**	34.09	32.70	-38.34
	EMG	short*	34.96	34.67	-46.61
		long**	34.49	34.21	-46.17
Freestyle	ECG		39.72	36.71	-39.72
	EMG		32.03	31.95	-49.23

*Note: * cable with 10cm; ** cable with 100cm.*

To characterize the real time and frequency response of the analog circuits (ECG and EMG), the gain was again reduced to 100 (In-Amp with unity Gain). The Figures 4.2a and 4.2b show the frequency response of the ECG and EMG circuits. The plots on top of these figures, illustrate the time response of each circuit when a synthesized chirp wave was applied (signal in which the frequency changes with time) with frequencies between 0 – 100 Hz and 0 – 500 Hz, respectively, with 1 second of duration, 25mVpp and offset of $V_{CC}/2$. As expected, the output signal is a chirp wave with attenuation at low and high frequencies. It illustrates the typical response of the filter applied (bandpass filter). On bottom of these figures, it is represented the frequency response of the signals plotted above (top figures), reinforcing what was described in advance.



(a) Frequency response of the ECG sensor. (b) Frequency response of the EMG sensor.
Bandwidth between $0.5 - 40\text{ Hz}$. Bandwidth between $10 - 400\text{ Hz}$.

Fig. 4.2. The frequency response of the ECG and EMG sensors.

In order to measure the time delay of each circuit (ECG and EMG), a transient analysis was performed. The time delay results obtained for the ECG and EMG circuit blocks were 2.337 and 0.146 seconds, respectively. The time delay is mostly delimited by the time constant ($\tau = RC$) of the integrator network at the first stage of the biosignal amplifier in both circuit blocks, as described in Section 3.1. Lastly, real ECG and EMG signals were acquired, as illustrated in Figure 4.3. For the ECG, we have placed the electrodes between the left and right hands (Lead I) using dry electrodes. For the EMG measurement we used the pre-gelled electrodes fixed over a muscle (biceps brachii).

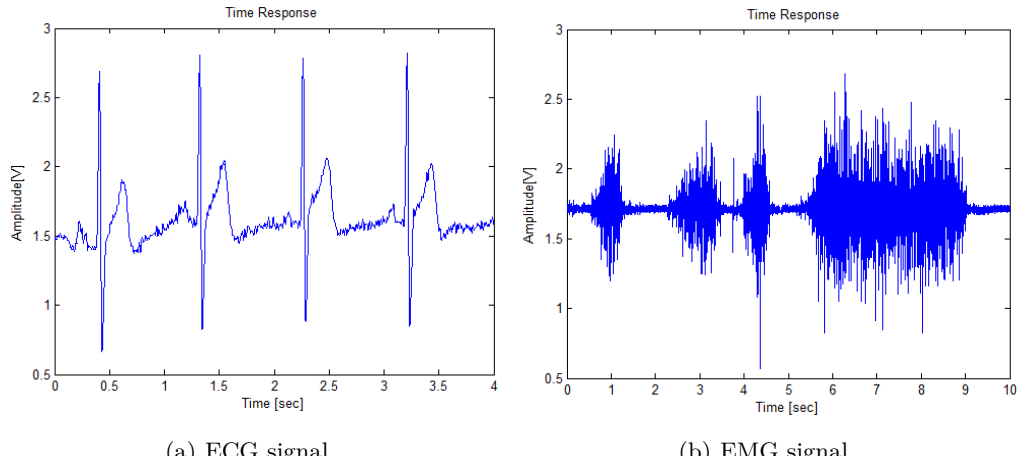
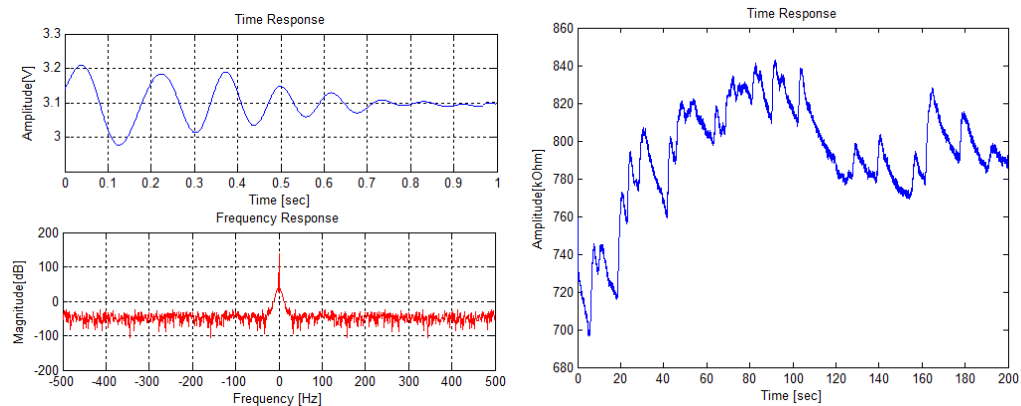


Fig. 4.3. Example of an ECG and an EMG signal acquired with the BITalino.

Similar to what was characterized in the ECG and EMG circuits, the time and frequency response was also evaluated for the EDA circuit design, as illustrated in Figure 4.4a). To perform this specific test, we have prototyped a Freestyle BITalino version with a proper firmware to actuate in a digital potentiometer (TPL0501 [73]) via SPI (Serial Peripheral Interface) bus. According to what was acquired in an analog channel, this system has changed the resistance of the digital potentiometer and then we could evaluate the response of the EDA sensor when the resistance (artificial skin resistance - R_{skin} in Figure 3.15) changed over time.

In Figure 4.4a) on top, it is illustrated the time response of the EDA circuit when a synthesized chirp wave with frequencies between 0 – 15 Hz, with 1 second of duration was injected to an analog channel of the BITalino (Freestyle version). As expected, the output signal of the EDA sensor is a chirp wave with attenuation at high frequencies. It illustrates the typical response of the filter designed (2nd order lowpass filter). Furthermore, on bottom of the Figure 4.4a) is illustrated the frequency response of this sensor and it reinforces what was described earlier.



(a) Frequency response of the EDA sensor. (b) Example of an EDA signal acquired by the Bandwidth between 0 – 5 Hz. BITalino.

Fig. 4.4. EDA sensor bandwidth characterization and signal example.

Another feature to be characterized in the EDA sensor was the full-scale range of the circuit. Experimental tests have shown that the sensor is able to measure skin resistances between $0\Omega \leq R_{skin} \leq 1M\Omega$, as expected in theory. Figure 4.4b) shows an example of a signal acquired using the EDA sensor.

The ACC and LUX sensors were also tested, and in Figure 4.5 we present a sample of each signal acquired. The accelerometer signal (Figure 4.5a) is from the z axis during a walking task,

in which the BITalino board was carried in the pocket (right leg). The light signal (Figure 4.5b) shows two consecutive instants where a light source was placed above the sensor.

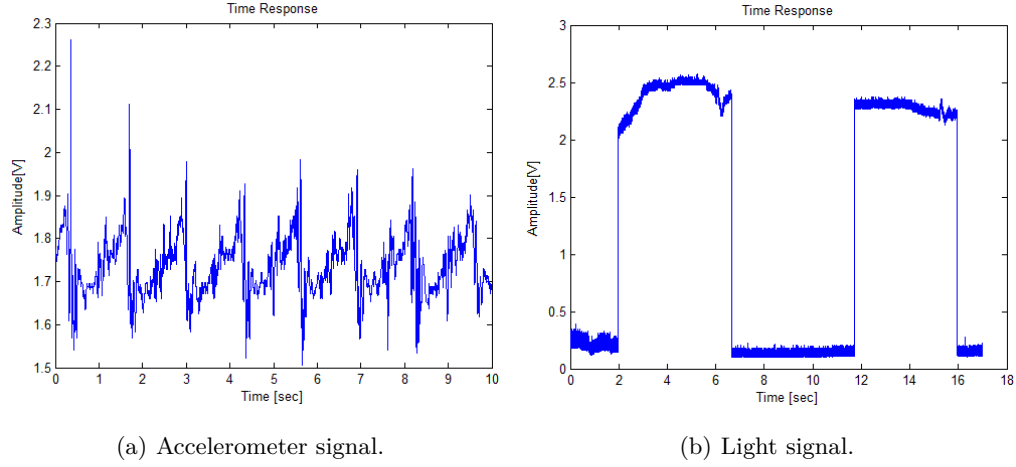


Fig. 4.5. Example of an ACC and LUX signals acquired with the BITalino.

The power consumption of the system is another important parameter that was evaluated. Tests with a Lithium-Ion/Lithium-Polymer battery with $3.7\text{ V} - 850\text{ mAh}$ have shown that the system has an autonomy of ≈ 17 hours when in real time acquisition (Live mode - 6 analog inputs + 4 digital inputs), and thus we conclude that the system consumes about $\approx 50\text{ mA}$, which corresponds at 0.185 W . Table 4.4 shows an overall information about the power consumption of each BITalino block.

Table 4.4. Overall information about power consumption of each BITalino block (approx. values).

	idle mode [mA]	live mode [mA]
ECG	-	4
EMG	-	4
EDA	-	2
LUX	-	0.05
ACC	-	0.35
LED	-	0(off); 10(on)
PWR	-	1
MCU	1	4
BT	10	40

Applications

In this Chapter we present several examples of applications built based on the developed platform that demonstrate its potential, as following described:

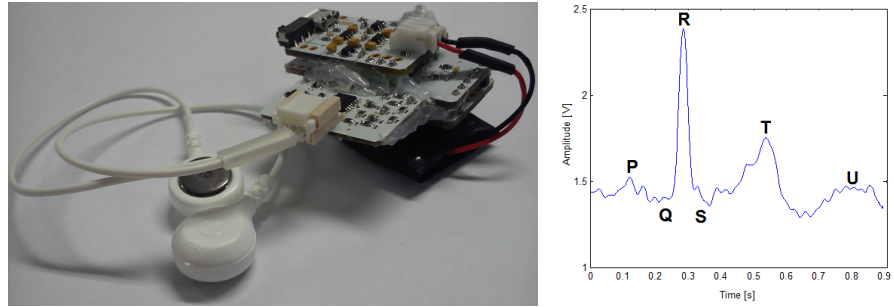
- *Beat-by-BIT* - an heartbeat detector that uses Electrocardiographic (ECG) signals to trigger a LED;
- *LightBIT and LockBIT* - a light controlled by the hands movements, using Accelerometric (ACC) signals, and a muscle controlled door lock, that uses Electromyographic (EMG) signals as a trigger;
- *"Mentir de Verdade"* - a didactic and interactive lie-detector setup based on Electrodermal Activity (EDA) signals and Heart Rate (HR);
- *FlowerBIT* - a twitting flower vase where we integrated non-BITalino sensors, that monitors the ambient light, soil moisture, relative humidity to the air and temperature, to check the "health" status of a flower.

5.1 Beat-by-BIT

The Beat-by-BIT is a heartbeat detection application, that uses Electrocardiographic (ECG) signals to trigger the onboard BITalino LED, as shown in Figure 5.1a.

This application uses a BITalino-Freestyle version (ECG sensor + MCU block + Power block + Battery). With a standalone firmware this system analyses the ECG signal to detect the R peaks within the P-QRS-T-U complexes (Figure 5.1b).

The strategy used for peak detection is adapted from the Slope Sum Function (SSF) algorithm to detect the onset of the arterial blood pressure proposed by [28]. As shown in Figure 5.2, the algorithm consists of three stages: a low-pass filter, a slope sum function, and a decision rule. The



(a) BITalino device.

(b) Prototypical ECG waveform.

Fig. 5.1. Beat-by-BIT device and ECG signal waveform.

ECG signal, x_n is the input of the low-pass filter, and y_n is the filtered ECG signal. The slope sum function converts y_n to a slope sum signal z_n . A decision rule is applied to z_n to determine the R peak instants, t , in time.

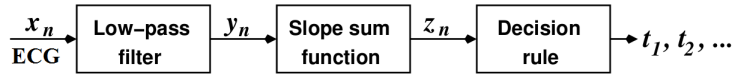


Fig. 5.2. Algorithm flow diagram. Redrawn and adapted from [28].

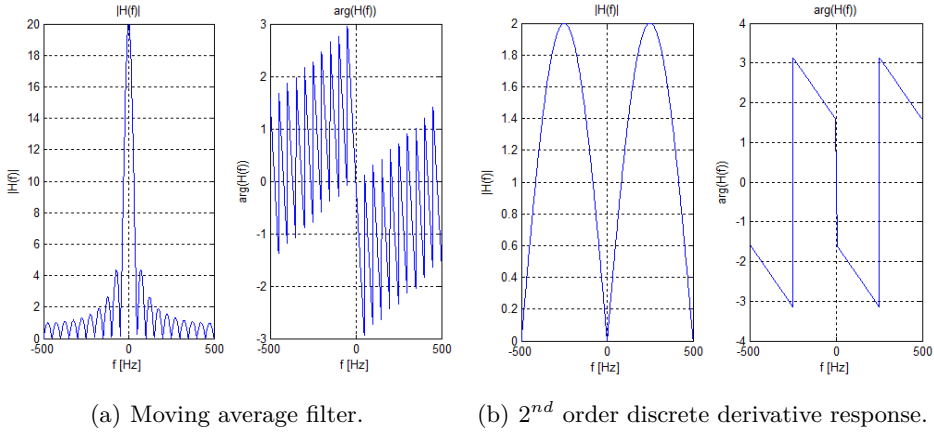
The purpose of the low-pass filter is to suppress high frequency noise (smoothing the ECG signal) that might affect the R peak detection. We used a moving average filter [74] which difference equation is given by the Equation 5.1, where x_n is the input signal, y_n is the output signal, and M is the number of points used in the moving average.

$$y[n] = \frac{1}{M} \sum_{j=0}^{M-1} x[n+j] \quad (5.1)$$

The frequency response is shown in Figure 5.3a for a sampling frequency of 1000 Hz. The $-3dB$ cut-off frequency is about 30 Hz and the gain is 20 at 0 Hz. The phase shift is 20 ms (20 samples).

The purpose of the slope sum function is to enhance the up slope of the R peak within the QRS complex and to suppress the remainder of the ECG signal. The slope sum function, z_n , at time n , is defined in Equation 5.2.

$$z_n = \sum_{k=n-j}^n \Delta u_k, \Delta u_k = \begin{cases} \Delta y_k & \Delta y_k > 0 \\ 0 & \Delta y_k \leq 0 \end{cases} \quad (5.2)$$



(a) Moving average filter.

(b) 2^{nd} order discrete derivative response.

Fig. 5.3. Frequency response of the filters applied.

Where $\Delta y_k = y_k - y_{k-2}$ is the 2^{nd} discrete derivative that results in a band pass filter, for which frequency response is illustrated in Figure 5.3b. The onset of the SSF signal coincides with the onset of the R peak because the SSF signal rises when the ECG signal (or noise not removed by filtering) rises.

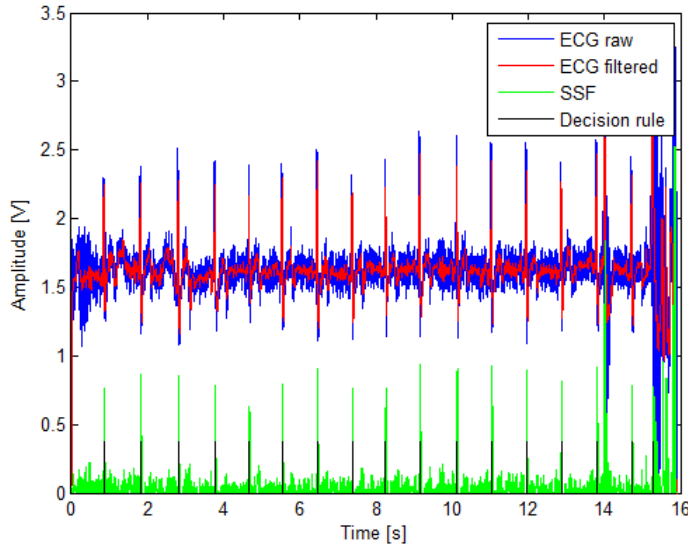


Fig. 5.4. Signals obtained at each stage of the adopted algorithm. The signal in blue, x_n , represents the raw ECG signal, the signal y_n , in red, is the low-pass filtered ECG signal, the signal z_n , in green, shows the SSF signal, and finally in black we show the validated R peaks.

Finally, a decision rule that allows the detection of each SSF pulse onset is applied. Firstly, we defined an amplitude interval by establishing empirical thresholds ($thd_{min} = 150$ and $thd_{max} = 400$), based on experimental studies and adapted from [75] for this given application. The algorithm rejects the values within the SSF signal that fall outside of the threshold interval, and to avoid double detection of the same pulse, the algorithm only accepts heartbeats between 40bpm and 180bpm . All new accepted SSF pulses are evaluated according to this "heartbeat" rule. Figure 5.4 illustrates all the signals resulted from each stage previously described.

5.2 LockBIT and LightBIT

The LockBIT is a muscle controlled door lock application, that uses Electromyographic (EMG) signals as a trigger, as shown in Figure 5.5a). The LightBIT is a gesture controlled light application, that is based on Accelerometry (ACC) to switch on/off a light when the BITalino board is moved.

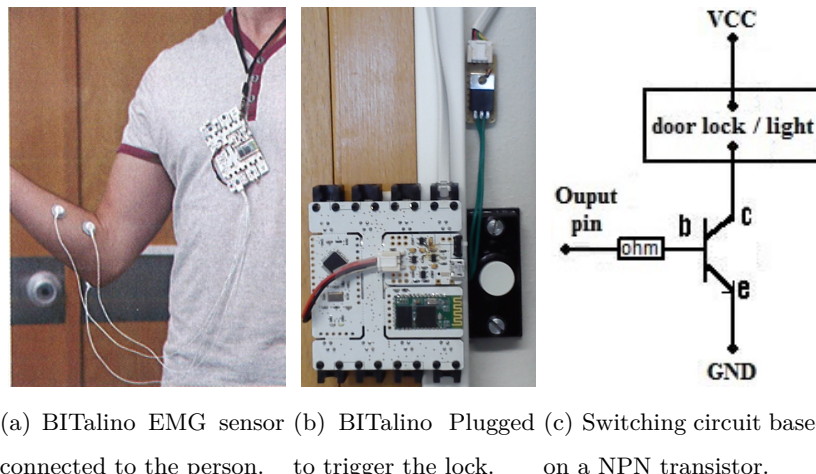


Fig. 5.5. The individual components of the LockBIT/LightBIT application.

These applications use two BITalino versions: a BITalino-Board to acquire the EMG or ACC signals and send the data to the base station through the Bluetooth module, and a BITalino-Plugged to trigger the door lock or the light circuits. A basic onset and motion detection software in Python running in the base station, allows real-time data processing from each BITalino. The data from the BITalino Board is analysed using a moving average window of 100 samples and validated against a threshold value previously defined. If the thresholding criteria is met, the

base station sends a command to the BITalino Plugged (as illustrated in Figure 5.5b) for the door lock example) to trigger one of the digital output ports, which is directly connected to the door lock or the light circuits via a switching circuit illustrated in Figure 5.5c.

5.3 "Mentir de Verdade"

A classical and well known use of electrophysiological signals is in the polygraph test, usually known as a "lie-detector". Typically, the instrument used to conduct polygraph tests consists of a physiological recorder that assesses four indicators of autonomic arousal [76]: heart rate, blood pressure, respiration, and electrodermal activity.



Fig. 5.6. Screenshot of the "Mentir de Verdade" application. Adapted with permission from [29].

Emotional situations, such as stress, anger, enjoyment, generate variations on the perspiration of the skin and variations of the heart rate as well. Those can be obtained through the Electrodermal Activity (EDA) signals and the Blood Volume Pulse (BVP) signals, respectively, since it is directly related to emotional variations, and as such, can be related with a lie. We addressed this issue in a pedagogical way, building a demonstration system where two persons are involved in a role-playing game based on the lying detector. This system was created for the module “Mentir de Verdade” to be used in an interactive non-intrusive setup and in an off-the-person approach, integrated in an upcoming exhibition (“Era uma vez...”) at the Pavilion of Knowledge - Ciência Viva [77], in Lisbon. The system is only concentrated on the physiological differences triggered by deceptive answers, based on the EDA signals measured by a BITalino

EDA sensor and the BVP signals are measured by an off-the-shelf sensor [78], attached, both attached to the hand, and using the BITalino as the platform for biosignals acquisition.

Figure 5.6 depicts an acquisition record of the obtained BVP and EDA signals, and also the Heart Rate (HR) variation over time. Each red timestamp indicates the instant when the game starts, while the grey region indicates the interval where the lie occurred. We refer the reader to [29] and [79] for additional characterization of this interactive "lie-detector" game.

5.4 FlowerBIT

The FlowerBIT is a platform for monitoring a flower, which collects information such as, soil moisture, air temperature, light and ambient humidity from additional analog sensors, to check the plant "health" state. In this application each analog sensor is directly connected to the BITalino Control block and the data is sent to the base station via Universal Serial Bus (USB) communication, as shown in Figure 5.7 (on left).



Fig. 5.7. FlowerBIT application.

The FlowerBIT software was based on the system architecture proposed in the SignalBIT framework. It consists of a back-end module in Python, for all the logic and communication operations, and a front-end in HTML5 and JavaScript languages to present the user interface. In this particular application, the back-end in Python is responsible for collecting the data and send each value to the front-end. Every 6 hours, the system sends a message about the plant "health" state to the Twitter [80], as shown in Figure 5.7 (on right). Figure 5.7 (at middle) shows the web-based front-end where each parameter being measured is displayed in real-time.

Conclusions and Future Work

This work presents a multimodal, versatile and low-cost (up to €150) platform , which consists of a hardware device slightly bigger than a "Credit Card" form factor, that integrates multiple measurement sensors for biosignal data acquisition, namely, Electrocardiography (ECG), Electromyography (EMG), Electrodermal Activity (EDA), and Accelerometry (ACC). It also includes a Light sensor and a Light-Emitting Diode (LED).

This board contributes for the strengthen of the physiological computing area, since it is a tool that enables biosignal enthusiasts to easily perform new applications. It integrates various types of biosignal sensors in a single board in a way that no other platform does. We shown several applications that demonstrate the potential of this board, namely: a Heartbeat-detector that uses Electrocardiographic (ECG) signals to trigger a LED; a light controlled by the wave of the hands, using Accelerometric (ACC) signals; a Muscle-controlled door lock, that uses Electromyographic (EMG) signals as a trigger; a didactic and interactive lie-detector setup that answers according to the emotional variations based on Electrodermal Activity (EDA) and Heart Rate (HR); and a twitting flower vase fitted with some additional non-BITalino sensors, that monitors the ambient light, soil moisture, relative humidity of the air and temperature, to check the "health" status of a flower.

BITalino is a board thought for the DIY community but its specifications allows a rigorous treatment of the biological information. The experimental results have shown that the data collected through the proposed system preserves the waveform properties and data integrity, that the system is accurate for real-time data acquisition, and that the analog front-end behaves according to what is defined in the reference literature as the characteristics of each signal. The BITalino was also designed in accordance with the main rules of the PCB manufacturers.

The BITalino board component options were mainly based on high versatility, low-power, performance and cost. The architecture was thought to enable the exchange of each of the main components. For communications, there are several other protocols that constitute a valid option as, Zigbee or ANT. The Bluethooth was chosen since it is one of the standard interfaces available in multiple devices (in our case the base station). For the MCU module, there are many other ICs that constitute a valid option as well, such as PIC and ARM families. The 8-bit AVR family resulted in a good choice in terms of performance and low power consumption. Since it is also widely used in the Arduino platform, we can also ensure that the Arduino users will have ease of use with BITalino as well.

Future work will be mainly focused on a slight review of some components that integrate the board in order to lower its price and provide an easier manufacturing process. Additionally, new modules will be designed, namely, analog sensors (Electroencephalography, Blood Volume Pressure, Oximetry, Skin Temperature, Respiratory Volume, Force), and an SD Card module for standalone signal acquisition. We also aim to improve the communication module for a Bluetooth Low Energy (BLE), to ensure less power consumption.

References

- [1] "Polar heart rate monitor.." http://en.wikipedia.org/wiki/Heart_rate_monitor.
- [2] "Wii vitality sensor controller.." <http://www.videogamesblogger.com/2009/06/05/wii-vitality-sensor-pictures.htm>.
- [3] "MYO - armband EMG sensor.." <https://www.thalmic.com/myo/>.
- [4] "Vitalidi - a biometric technology based on ECG signal.." <http://www.vitalidi.com/>.
- [5] R. P. Jaakkko Malmivuo, "*The Heart*", in *Bioelectromagnetism - Principles and Applications of Bioelectric and Biomagnetic Fields*. Oxford University Press, New York, 1995.
- [6] R. P. Jaakkko Malmivuo, "*12-Lead ECG System*", in *Bioelectromagnetism - Principles and Applications of Bioelectric and Biomagnetic Fields*. Oxford University Press, New York, 1995.
- [7] "ECG precordial leads.." <http://www.cixip.com/index.php/page/content/id/192>.
- [8] "EMG signal image." http://www.medicalexhibits.com/medical_exhibits.php?exhibit=10080_04X&query=electromyogram%20nerve%20conduction%20velocity%20tests%20leg%20performed.
- [9] "EMG electrodes placement.." http://wg11.sc29.org/mpeg-v/?page_id=2356.
- [10] M. K. B. A. Cornelia Kappeler-Setz, Johannes Schumm and G. Troster, "Towards long term monitoring of electrodermal activity in daily life," *International workshop on Ubiquitous Healthcare and Supporting Technologies*, 2010.
- [11] N. Jia, "Fall detection application by using 3-axis accelerometer adxl345," *Application Note (AN-1023) from Analog Devices*, 2009.
- [12] "Accelerometry signal example.." <http://www.biosignalsplus.com/downloads/sensors/accel.pdf>.

- [13] J. G. Webster, "*Biopotential Electrodes*", in *Medical Instrumentation – Application and Design*. Wiley, 4th ed., 2009.
- [14] R. P. Jaakko Malmivuo, "*The Electrodermal Response*", in *Bioelectromagnetism - Principles and Applications of Bioelectric and Biomagnetic Fields*. Oxford University Press, New York, 1995.
- [15] A. Baba and M. J. Burke, "Measurement of the electrical properties of ungelled ecg electrodes," *International Journal of Biology and Biomedical Engineering*, vol. 2, no. 3, 2008.
- [16] "Ag-AgCl electrodes.." http://image.tradevv.com/2008/09/05/ecgelectrode_156520_600/ecg-electrodes-carbon-snap-ag-agci-sensor-low-impedance-solid-medical-conductive-gel.jpg.
- [17] "ECG noise from motion artifacts.." http://www.wikipediacom/index.php/File:Noise_move.png.
- [18] D. Prutchi and M. Norris, "*Biopotential Amplifiers*", in *Design and Development of Medical Electronic Instrumentation*. Wiley, 2005.
- [19] J. G. Webster, "*Biopotential Amplifiers*", in *Medical Instrumentation Application and Design*. Wiley, 4th ed., 2009.
- [20] C. Kitchen and L. Counts, *A Designer's Guide to Instrumentation Amplifiers*. Analog Devices, 3rd ed., 2006.
- [21] T. Instruments, *Micro-Power, Zero-Drift, Rail-to-Rail Out Instrumentation Amplifier datasheet(INA333)*. Texas Instruments, 2008.
- [22] ATMEL, *Micro-Controller Unit datasheet(ATmega328P)*. ATMEL, 2009.
- [23] MICREL, *150mA Low-Noise LDO Regulator datasheet(MIC5205)*. MICREL, 2000.
- [24] T. Instruments, *Low-Noise, High PSRR, RF 200mA, Low-dropout Regulator datasheet(TPS73001)*. Texas Instruments, 2004.
- [25] T. Instruments, *Single-Supply, Rail-to-Rail Operational Amplifier datasheet(OPA364)*. Texas Instruments, 2003.
- [26] Microship, *Miniature Single-Cell, Fully Integrated Li-Ion, Li-Polymer Charge Management Controller datasheet(MCP73831)*. Microship, 2008.
- [27] "Single cell Polymer Lithium Ion Battery.." <https://www.sparkfun.com/products/341>.
- [28] W. Zong, T. Heldt, G. B. Moody, and R. G. Mark, "An open-source algorithm to detect onset of arterial blood pressure pulses," 2003.

- [29] A. P. Alves, H. Silva, A. Lourenço, A. Fred, I. Montalvão, and L. Alegre, “Uncovering Lying Detection using Blood Volume Pulse and Electrodermal Activity,” in *Proceedings of the 9th Conference on Telecommunications (ConfTele)*, 2013.
- [30] J. P. Clarys and J. Cabri, “Electromyography and the study of sports movements: A review.,” *J Sports Sci*, vol. 11, pp. 379–448+, 1993.
- [31] V. Stanford, “Biosignals offer potential for direct interfaces and health monitoring,” *Pervasive Computing, IEEE*, vol. 3, pp. 99 – 103, jan.-march 2004.
- [32] B. Graimann, B. Allison, and G. Pfurtscheller, eds., *Brain-Computer Interfaces*. Springer, 2011.
- [33] A. Lourenço, H. Silva, and A. Fred, “Unveiling the biometric potential of Finger-Based ECG signals,” *Computational Intelligence and Neuroscience*, vol. 2011, 2011.
- [34] F. Agrafioti, “ECG in Biometric Recognition: Time Dependency and Application Challenges,” *PhD Thesis*, 2011.
- [35] M. Schwartz and F. Andrasik, *Biofeedback: A Practitioner’s Guide*. The Guilford Press, 3rd ed., June 2005.
- [36] A. Freivalds, *Biomechanics of the Upper Limbs: Mechanics, Modeling and Musculoskeletal Injuries, Second Edition*. CRC Press, 2 ed., Feb. 2011.
- [37] F. S. Qiang Fang and I. Cosic, eds., *A Mobile Device Based ECG Analysis System, Book edited by: Eugenia G. Giannopoulou*.
- [38] “Arduino.” <http://www.arduino.cc/>.
- [39] M. Banzi, *Getting Started with Arduino*. Make Books, Oct. 2009.
- [40] P. Bender and K. Kussmann, “Arduino based projects in the computer science capstone course,” *J. Comput. Sci. Coll.*, vol. 27, pp. 152–157, May 2012.
- [41] J. Sarik and I. Kymmissis, “Lab kits using the arduino prototyping platform,” in *IEEE Frontiers in Education Conference*, 2010.
- [42] L. Buechley and M. Eisenberg, “The lilypad arduino: Toward wearable engineering for everyone,” *IEEE Pervasive Computing*, vol. 7, no. 2, pp. 12–15, 2008.
- [43] “LilyPad Arduino.” <http://arduino.cc/en/Main/ArduinoBoardLilyPad>.
- [44] “Raspberry Pi.” <http://www.raspberrypi.org/>.
- [45] J. G. Webster, “*The origin of Biopotentials*”, in *Medical Instrumentation Application and Design*. Wiley, 4th ed., 2009.
- [46] T. Boone and L. Birnbaum, “Basic concepts in sports biomechanics,” *PhD, MPH, FASEP, EPC*, 2009.

- [47] P. P. Correia, ed., *Aparelho Locomotor: Função Neuromuscular e Adaptações à Atividade Física*. Faculdade de Motricidade Humana - Edições FMH, 2nd ed., 2012.
- [48] A. Merlo and I. Campanini, "Technical aspects of surface electromyography for clinicians,"
- [49] W. Boucsein, ed., *Electrodermal Activity*. Springer, 2012.
- [50] J. G. Webster, "Basic Concepts of Medical Instrumentation", in *Medical Instrumentation Application and Design*. Wiley, 4th ed., 2009.
- [51] "Acceleration definition.." <http://physics.info/acceleration/>.
- [52] C. Payton and R. Bartlett, *Biomechanical Evaluation of Movement in Sport and Exercise*. Routledge, 1st ed. 208 ed., 2008.
- [53] C. E. P. Armir Bujari, Bogdan Licar, "Movement pattern recognition through smart-phone's accelerometer," *Consumer Communications and Networking Conference (CCNC), 2012 IEEE*, 2012.
- [54] "Nintendo Wii." <http://www.nintendo.com/wii>.
- [55] T.-S. K. Myong-Woo Lee, Adil Mehmood Khan, "A single tri-axial accelerometer-based real-time personal life log system capable of human activity recognition and exercise information generation," *Springer-Verlag London Limited 2011*, May 2011.
- [56] E. Morin, *ELEC 408 - Electrodes and Electrode Theory*. Queen's University, 2009.
- [57] Y. Gondran, Siebert and Novakov, *Noise of surface biopotential electrodes based on NASICON ceramic and Ag-AgCl*. Med. Biol. Eng. Comput., 1996.
- [58] Y. Gondran, Siebert and Novakov, *Dry electrode based on NASICON ceramic for surface biopotential measurement—skin-electrode impedance and noise*. Innov. Tech. Biol. Med., 1995.
- [59] P. Huigen and Grimbergen, *Investigation into the origin of the noise of surface electrodes*. Med. Biol. Eng. Comput., 2002.
- [60] A. T. E. M. M. A. M. Roberto Merletti, Alberto Botter, *Technology and instrumentation for detection and conditioning of the surface electromyographic signal: State of the art*. Clinical Biomechanics 24, 2009.
- [61] R. P. Jaakko Malmivuo, *Bioelectromagnetism - Principles and Applications of Bioelectric and Biomagnetic Fields*. Oxford University Press, New York, 1995.
- [62] W. Boucsein, *Electrodermal Activity*. Springer, 2nd ed. 2012 ed., 2011.
- [63] D. A. Winter, *Biomechanics and Motor Control of Human Movement*. Wiley, 3 ed., 2004.
- [64] A. Devices, *Low Cost, Low Noise, CMOS, Rail-to-Rail Out Operational Amplifier datasheet(INA333)*. Analog Devices, 2011.

- [65] J. G. W. James C. Huhta, “60-hz interference in electrocardiography,” *IEEE Transactions on Biomedical Engineering*, 1973.
- [66] A. Devices, *Low Power, Small, 3-Axis $\pm 3g$ Accelerometer datasheet(ADXL335)*. Analog Devices, 2009.
- [67] V. Semiconductors, *Ambient Light Sensor datasheet(TEMT6000)*. Vishay Semiconductors, 2004.
- [68] “Wireless Healthcare devices..” <http://www.bluetooth.com/Pages/Medical.aspx>.
- [69] U. A. Bakshi and A. V. Bakshi, eds., *Measurements and Instrumentation*. Technical Publications Pune, 3rd ed., 2009.
- [70] A. P. A. Alves, H. Silva, A. Lourenço, and A. L. N. Fred, “SignalBIT: A web-based platform for real-time biosignal visualization and recording,” in *International Conf. on Signal Processing and Multimedia Applications*, July 2013.
- [71] H. P. da Silva, C. Carreiras, A. Lourenço, and A. Fred, “Off-the-person electrocardiography,” in *1st International Congress on Cardiovascular Technologies*, 2013.
- [72] B. Baker, “A glossary of analog-to-digital specifications and performance characteristics,” *Texas Instruments - Application Report*, 2011.
- [73] T. Instruments, *256 Taps Single Channel Digital Potentiometer With SPI Interface datasheet(TPL0501)*. Texas Instruments, 2011.
- [74] S. W. Smith, ed., *The Scientist and Engineer’s Guide to Digital Signal Processing*. California Technical Publishing, 2nd ed., 1999.
- [75] F. Canento, A. Lourenço, H. Silva, and A. Fred, “On real time ecg segmentation algorithms for biometric applications,” *Int’l Conference on Bio-inspired Systems and Signal Processing (BIOSIGNALS)*, pp. 228–235, 2013.
- [76] L. Geddes, “The truth shall set you free [development of the polygraph],” *Engineering in Medicine and Biology Magazine, IEEE*, vol. 21, pp. 97 –100, may-june 2002.
- [77] “The Pavilion of Knowledge - Ciência Viva..” <http://www.pavconhecimento.pt/home/>.
- [78] “Off-the-shelf pulse sensor..” <https://www.pulsesensor.com>.
- [79] H. Silva, A. P. Alves, A. Lourenço, A. Fred, I. Montalvão, and L. Alegre, *Towards the Detection of Deception in Interactive Multimedia Environments*, vol. 7947, pp. 65–76. Human-Computer Interaction and Knowledge Discovery in Complex, Unstructured, Big Data Lecture Notes in Computer Science, Springer, 2013.
- [80] “TeamBIT Twitter page..” https://twitter.com/_TeamBIT_.